SYNTHETIC APERTURE IMAGING OF DIRECTION AND FREQUENCY DEPENDENT REFLECTIVITIES

LILIANA BORCEA*, MIGUEL MOSCOSO †, GEORGE PAPANICOLAOU‡, AND CHRYSOULA TSOGKA§

Abstract. We introduce a synthetic aperture imaging framework that takes into consideration directional dependence of the reflectivity that is to be imaged, as well as its frequency dependence. We use an ℓ_1 minimization approach that is coordinated with data segmentation so as to fuse information from multiple sub-apertures and frequency sub-bands. We analyze this approach from first principles and assess its performance with numerical simulations in an X-band radar regime.

Key words. synthetic aperture imaging, reflectivity, minimal support optimization.

1. Introduction. We introduce and analyze a novel algorithm for synthetic aperture radar (SAR) imaging, where a moving receive-transmit platform probes a remote region with signals $f(t)$ and records the scattered waves. The platform spans a large synthetic aperture so that high resolution images of the region may be obtained by processing the recorded data. A related application is inverse synthetic aperture radar (ISAR), where the receive-transmit antenna is stationary, and the synthetic aperture is due to the motion of an unknown scatterer. If this motion is known or can be estimated, the problem can be restated mathematically as SAR imaging of the scatterer, using the reference frame that moves with it.

A schematic of the SAR imaging setup is in Figure 1.1. The recordings $u(s,t)$ at the moving receive-transmit platform depend on two time variables: the slow time s and the fast time t. The slow time parametrizes the trajectory of the platform, and it is discretized in uniform steps h_s, called the pulse repetition rate. At time s the platform is at location $\vec{r}(s)$. It emits the signal $f(t)$ and receives the backscattered returns $u(s,t)$. The fast time t runs between consecutive signal emissions $t \in (0, h_s)$, and we assume a separation of time scales: The duration of $f(t)$ is smaller than the round trip travel time of the waves between the sensor and the imaging region, and the latter is smaller than h_s.

In the usual synthetic aperture image formulation the reflectivity is modeled as a two dimensional function of location $\vec{y}$ on a surface of known topography, say flat for simplicity. The assumption is that each point on the surface reflects the waves the same way in all directions, independent of the direction and frequency of the incident waves. This simplifies the imaging process and makes the inverse problem formally determined: the data are two-dimensional and so is the unknown reflectivity function.

The reflectivity can be reconstructed by the reverse time migration formula [20, 10, 15, 7]

$$\mathcal{I}(\vec{y}) = \sum_j \int dt\, u(s_j, t)\overline{f\big(t - 2\tau(s_j, \vec{y})\big)}. \tag{1.1}$$

Here s_j are the slow time emission-recording instants, spaced by h_s, and the image is formed by superposing over the platform trajectory the data $u(s_j, t)$, match-filtered with the time reversed emitted signal $f(t)$, delayed by the roundtrip travel time $2\tau(s_j, \vec{y}) = 2|\vec{r}(s_j) - \vec{y}|/c$ between the platform location $\vec{r}(s_j)$ and the imaging point $\vec{y}$. The bar denotes complex conjugate and c is the wave speed in the medium which is assumed homogeneous.

The assumption of an isotropic reflectivity may not always be justified in applications. Backscatter reflectivities are in general functions of five variables: the location $\vec{y}$ on the known (flat) surface, the two angles of incidence and the frequency. Thus, the inverse problem is underdetermined and we cannot expect a reconstruction of the five dimensional reflectivity with a migration approach. Direct application of (1.1) will produce low-resolution images of some effective, position-dependent reflectivity, and there will be no information about the directivity and frequency dependence of the actual reflectivity.

The reconstruction of frequency dependent reflectivities with synthetic aperture radar has been considered in [8], where Doppler effects are shown to be useful in inversion, and in [21, 11], where data are segmented over frequency sub-bands, and then images are formed separately, for each data subset. Data segmentation is a natural idea, and we show here how to use it for reconstructing both frequency and direction dependent reflectivities.

The main result in this paper is the introduction and analysis of an algorithm for imaging direction and frequency dependent reflectivities of strong, localized scatterers. This algorithm is based on ℓ_1 optimization.

---

*Department of Mathematics, University of Michigan, Ann Arbor, MI 48109 `borcea@umich.edu`

†Gregorio Millán Institute, Universidad Carlos III De Madrid, Madrid 28911, Spain `moscoso@math.uc3m.edu`

‡Stanford Mathematics Department, 450 Serra Mall Bldg. 380, Stanford CA 94305 `papanico@math.stanford.edu`

§Mathematics and Applied Mathematics, University of Crete and IACM/FORTH, GR-71409 Heraklion, Greece `tsogka@uoc.gr`
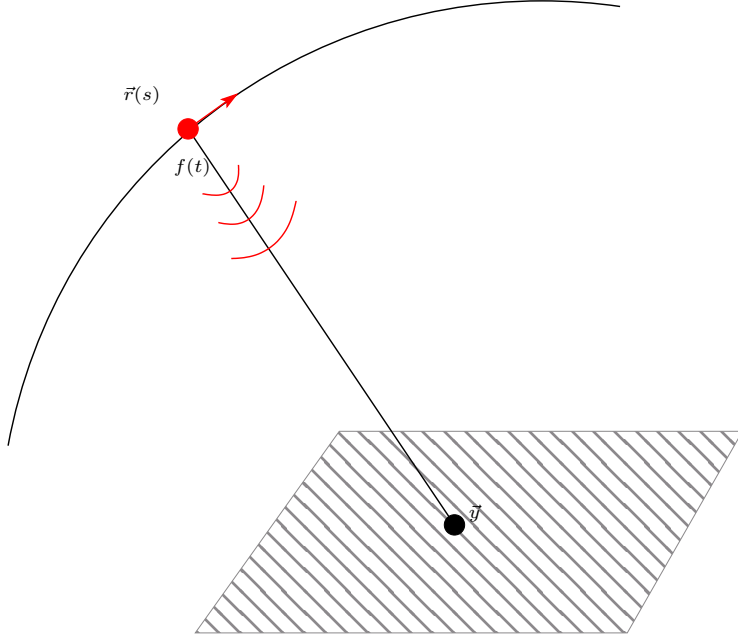
FIG. 1.1. *Setup for imaging with a synthetic aperture.*

It reconstructs reflectivities of localized scatterers by seeking among all those that fit the data model the ones with minimal spatial support. Array imaging algorithms based on ℓ_1 optimization are proposed and analyzed in [1, 18, 5, 4, 14, 13, 2]. They consider only isotropic, frequency independent reflectivities.

A direct extension of ℓ_1 optimization methods to imaging direction and frequency dependent reflectivities amounts to solving a grand optimization problem for a very long vector $\boldsymbol{\rho}$ of unknowns, the discretized reflectivity over spatial locations on the imaging grid, the angles of incidence/backscatter and the frequency. It has considerable computational complexity because of the high dimension of the space in which the discretized reflectivity vector lies. It also does not take into account the fact that many unknowns are tied to the same spatial location points within the discretized image window.

The synthetic aperture imaging algorithm introduced in this paper is designed to reconstruct efficiently direction and frequency dependent reflectivities by combining two main ideas: The first is to divide the data over carefully calibrated sub-apertures and frequency sub-bands, and solve an ℓ_1 optimization problem to estimate the reflectivity for each data subset. Data segmentation is useful assuming that the reflectivity changes continuously with the direction of probing and the frequency, so that we can approximate it by a piecewise constant function, pointwise in the imaging window. Over a sub-aperture of small enough linear size a, the platform receives scattered waves from a narrow cone with opening angle of the order a/L, where L is the distance from the platform to the imaging window, and we can approximate the reflectivity by that at the center angle. Similarly, we can approximate the reflectivity by a constant over a small enough frequency sub-band. Then, we can use ℓ_1 optimization to estimate the reflectivity as a function of location for each data subset. The size of the sub-apertures and sub-bands determine the resolution of the reconstruction. The larger they are, the better the expected spatial resolution of the reflectivity. But the resolution is worse over direction and frequency dependence. The calibration of the data segmentation over sub-apertures and sub-bands reflects this trade-off. The second idea combines the ℓ_1 optimizations by seeking reflectivities that have common spatial support. Instead of a single vector $\boldsymbol{\rho}$, the unknown is a matrix with columns of spatially discretized reflectivities. Each column corresponds to a direction of probing from a sub-aperture and a central frequency in a sub-band. The values of the entries in the columns are different, but they are zero (negligible) in the same rows. Moreover, the forward model, which is derived here from first principles, maps each column of the reflectivity matrix to the entries in the data subsets via one common reflectivity-to-data model matrix. The optimization can then be carried out within the multiple measurement vector (MMV) formalism described in [16, 9, 23, 22].

The MMV formalism is used for solving matrix-matrix equations for an unknown matrix variable whose columns share the same support but have possibly different nonzero values. We show in this paper how to reduce the synthetic aperture imaging problem to an MMV format. The columns of the unknown matrix are associated

with the discretized spatial reflectivities for different directions and frequencies. The solution of the MMV problem can be obtained with a matrix (2,1)-norm minimization where one seeks to minimize the ℓ_1 norm of the vector formed by the ℓ_2 norms of the rows of the unknown reflectivity matrix. The solutions obtained this way preserve the common support of the columns of the unknown matrix.

This paper is organized as follows. We begin in section 2 with the formulation of the imaging problem. We derive the data model, describe the complexity of the inverse problem, and motivate our imaging approach. The foundation of this approach is in section 3, where we show how to reduce the imaging problem to an MMV format. The imaging algorithm is described in section 4 and its performance is assessed with numerical simulations in section 5. The presentation in sections 2-5 uses the so-called start stop approximation, which neglects the motion of the receive-transmit platform over the duration of the fast time data recording window. This is for simplicity and also because the approximation holds in the X-band radar regime used in the numerical simulations. However, the imaging algorithm can include Doppler effects due to the motion of the receive-transmit platform, as explained in section 6. We end with a summary in section 7.

2. Formulation of the imaging problem. The data model is described in section 2.1. Then, we review briefly imaging of isotropic reflectivity functions via migration and ℓ_1 optimization in section 2.2. The formulation of the problem for direction and frequency dependent reflectivities is in section 2.3

2.1. Synthetic aperture data model. In synthetic aperture imaging we usually assume that the data $u(s,t)$, depending on the slow time s and the fast time t, can be modeled with the single scattering approximation. For an isotropic and frequency independent reflectivity function $\rho = \rho(\vec{y})$ we have

$$u(s,t) = \int \frac{d\omega}{2\pi} \widehat{u}(s,\omega) e^{-i\omega t}, \tag{2.1}$$

with Fourier transform $\widehat{u}(s,\omega)$ given by

$$\widehat{u}(s,\omega) \approx k^2 \widehat{f}(\omega) \int_\Omega d\vec{y}\, \rho(\vec{y}) \frac{\exp\left[2i\omega\tau(s,\vec{y})\right]}{(4\pi|\vec{r}(s) - \vec{y}|)^2}. \tag{2.2}$$

Here $k = \omega/c$ is the wavenumber and the integral is over points $\vec{y}$ in Ω, the support of ρ. The model (2.2) uses the so-called start-stop approximation, where the platform is assumed stationary over the duration of the fast time recording window. We use this approximation throughout most of the paper for simplicity, and because it holds in the X-band radar regime considered in the numerical simulations. However, the results extend to other regimes, where Doppler effects may be important, as explained in section 6.

The inverse problem is to invert relation (2.2) and thus estimate $\rho(\vec{y})$, given $u(s_j,t)$ at the slow time samples $s_j = (j-1)h_s$, for $j = 1, \ldots, N_s$. Here h_s is the slow time sample spacing. The inversion is usually done by discretizing (2.2), to obtain a linear system of equations for the unknown vector $\boldsymbol{\rho}$ of discretized reflectivities. The support Ω in (2.2) is not known, so the inversion is done in a bounded search domain $\mathcal{Y}$ on the imaging surface, assumed flat. We call $\mathcal{Y}$ the image window. The reconstruction of $\boldsymbol{\rho}$ in $\mathcal{Y}$ is a solution of the linear system, as we review briefly in section 2.2.

The discretization of $\mathcal{Y}$ is adjusted so that it is comensurate with the expected resolution of the image in range and cross-range. The range direction is the projection on the imaging plane of the unit vector pointing from the imaging location $\vec{y} \in \mathcal{Y}$ to the platform location. The cross-range direction is orthogonal to range. It is well known in imaging that the range resolution is determined by the accuracy of travel time estimation, which in term is determined by the temporal support of $f(t)$. Thus, it useful to have a short pulse $f(t)$ whose support is of order $1/B$, where B is the bandwidth. The range resolution with such pulses is of order c/B. The cross-range resolution is proportional to the central wavelength, which is why the emitted signals are typically modulated by high carrier frequencies $\omega_o/(2\pi)$. If L is a typical distance between the platform and the imaging window and $\mathcal{A}$ is the length of the flight path, so that the platform receives waves within a cone of opening angle $\mathcal{A}/L$, the cross-range resolution is of the order $\lambda_o L/\mathcal{A}$, where $\lambda_o = 2\pi c/\omega_o$ is the carrier wavelength. We assume that $\omega_o \gg B$, which is usually the case in radar.

In synthetic aperture imaging applications like SAR, the platform emits relatively long signals $f(t)$ so as to carry sufficient energy to generate strong scatter returns, and thus high signal to noise ratios. Examples of such signals are chirps, whose frequency changes over time in an interval centered at the carrier frequency $\omega_o/(2\pi)$. To improve the precision of travel time estimation, and therefore range resolution, the returns $u(s_j,t)$ are compressed in time via match-filtering with the time reversed emitted signal [20]. Moreover, to remove the large phases and

therefore avoid unnecessarily high sampling rates for the returns, the data are migrated via travel time delays calculated with respect to a reference point $\vec{y}_o$ in the imaging window. The combination of these two data pre-processing steps is called down-ramping.

For the purposes of this paper it suffices to assume that $f(t)$ is a linear chirp, in which case the Fourier transform $|\widehat{f}(\omega)|^2$ of the compressed signal has approximately the simple form

$$|\widehat{f}(\omega)| \approx |\widehat{f}(\omega_o)| 1_{[\omega_o-\pi B, \omega_o+\pi B]}(\omega), \tag{2.3}$$

where $1_{[\omega_1,\omega_2]}(\omega)$ denotes the indicator function of the frequency interval $[\omega_1, \omega_2]$. The down-ramped returns are

$$\int dt' \, u\Big(s, t-t'+2\tau(s,\vec{y}_o)\Big)\overline{f(-t')} = \int \frac{d\omega}{2\pi} \, \overline{\widehat{f}(\omega)} \widehat{u}(s,\omega) e^{-i\omega\left[t+2\tau(s,\vec{y}_o)\right]}, \tag{2.4}$$

and we let $\mathbf{d}$ be the vector of the samples of its Fourier transform

$$\mathbf{d} = (d(s_j,\omega_l))_{j=1,\dots N_s, l=1,\dots,N_\omega}, \qquad d(s,\omega) = \overline{\widehat{f}(\omega)}\widehat{u}(s,\omega) e^{-2i\omega\tau(s,\vec{y}_o)}. \tag{2.5}$$

The size of the vector $\mathbf{d}$ is $N_s N_\omega$.

The linear relation between the unknown reflectivity vector $\boldsymbol{\rho}$ and the down-ramped data vector $\mathbf{d}$ follows from (2.5) and (2.2). We write it as

$$\mathbf{A}\boldsymbol{\rho} = \mathbf{d}, \tag{2.6}$$

where the entries in $\boldsymbol{\rho} \in \mathbb{C}^Q$ are proportional to $\rho(\vec{y}_q)$, with $\vec{y}_q$ the Q discretization points of the image window $\mathcal{Y}$, and with the constant of proportionality taken to be the area of a grid cell. The reflectivity $\boldsymbol{\rho}$ is mapped by the reflectivity-to-data matrix $\mathbf{A} \in \mathbb{C}^{N_S N_\omega \times Q}$ to the data $\mathbf{d}$. The assumption of frequency independent reflectivity leads to a set of decoupled systems of equations $\mathbf{A}(\omega_l)\boldsymbol{\rho} = \mathbf{d}(\omega_l)$ indexed by the frequency ω_l, where the entries of the $N_s \times Q$ matrices $\mathbf{A}(\omega_l)$ are

$$\mathbf{A}_{j,q}(\omega_l) = \frac{k_l^2 |\widehat{f}(\omega_l)|^2}{(4\pi|\mathbf{r}(s_j) - \vec{y}_q|)^2} e^{2i\omega_l \left[\tau(s_j,\vec{y}_q) - \tau(s_j,\vec{y}_o)\right]}. \tag{2.7}$$

Here $k_l = \omega_l/c$, $l = 1, \dots, N_\omega$, $j = 1, \dots, N_s$, and $q = 1, \dots, Q$.

2.2. Imaging isotropic reflectivities. Imaging of the isotropic reflectivities amounts to inverting the linear system (2.6). When this system is underdetermined, there are two frequently used choices for picking a solution: either minimize the Euclidian norm of $\boldsymbol{\rho}$ or its ℓ_1 norm. The first choice gives

$$\boldsymbol{\rho} = \mathbf{A}^\dagger \mathbf{d}, \tag{2.8}$$

where $\mathbf{A}^\dagger$ is the pseudo-inverse of $\mathbf{A}$. If $\mathbf{A}$ is full row rank, $\mathbf{A}^\dagger = \mathbf{A}^*(\mathbf{A}\mathbf{A}^*)^{-1}$. The inversion formula (2.8) also applies to overdetermined problems, where $\boldsymbol{\rho}$ is the least squares solution and $\mathbf{A}^\dagger = (\mathbf{A}^*\mathbf{A})^{-1}\mathbf{A}^*$, for full column rank $\mathbf{A}$. The choice of the imaging window $\mathcal{Y}$ and its discretization is an essential part of the imaging process and, depending on the objectives and available prior information, we may be able to control whether the system (2.6) is overdetermined or not. We explain in Appendix B that by discretizing $\mathcal{Y}$ in steps commensurate with expected resolution limits we can make the columns of $\mathbf{A}$ nearly orthogonal. This means that in the overdetermined case $\mathbf{A}^*\mathbf{A}$ is close to a diagonal matrix. We also shown in Appendix B that in the underdetermined case, for coarse enough sampling of the slow time s and frequency ω, the rows of $\mathbf{A}$ are nearly orthogonal, and therefore $\mathbf{A}\mathbf{A}^\star$ is close to a diagonal matrix. Thus, in both cases, $\mathbf{A}^\dagger$ is approximately $\mathbf{A}^\star$ up to multiplicative factors, and we can therefore image the support of $\boldsymbol{\rho}$ with $\mathbf{A}^*\mathbf{d}$. This is in fact the migration formula (1.1) written in the Fourier domain, up to a geometrical factor, since the amplitude in (2.7) is approximately constant for platform trajectories that are shorter than the imaging distance and for bandwidths $B \ll \omega_o$.

If we know that the imaging scene consists of a few strong, localized scatterers, as we assume here, a better estimate of $\boldsymbol{\rho}$ is given by the optimization

$$\min \|\boldsymbol{\rho}\|_1 \quad \text{such that} \quad \|\mathbf{A}\boldsymbol{\rho} - \mathbf{d}\|_2 \le \epsilon. \tag{2.9}$$

Here ϵ is an error tolerance, commensurate with the noise level in the data, and $\|\cdot\|_1$ and $\|\cdot\|_2$ are the ℓ_1 and the Euclidian norm, respectively. We refer to [1, 18, 4, 14, 13] for studies of imaging with ℓ_1 optimization. The main result in this context is that when there is no noise so that $\epsilon = 0$, the reflectivities are recovered exactly provided that the inner products of the normalized columns of $\mathbf{A}$ are sufficiently small. An extension of the optimization to nonlinear data models that account for multiple scattering effects in $\mathcal{Y}$, is considered in [5]. A resolution study of imaging with ℓ_1 optimization is in [2].
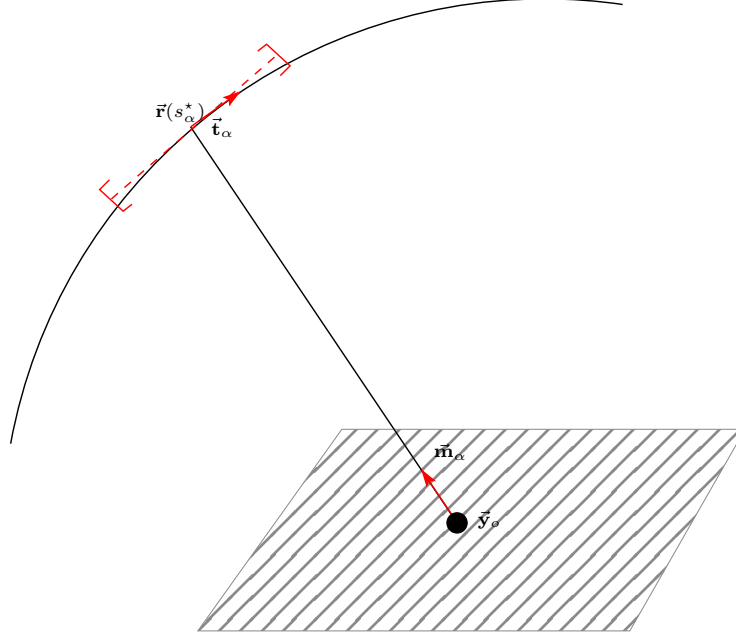
FIG. 3.1. *Scematic of the geometry for one sub-aperture centered at the location $\vec{\mathbf{r}}(s_q^\star)$ of the receive-transmit platform.*

2.3. Imaging direction and frequency dependent reflectivities. In general, backscatter reflectivities are functions of five variables: the location $\vec{\mathbf{y}} \in \mathcal{Y}$, the unit direction vector $\vec{\mathbf{m}}$ and the frequency ω. Hence,

$$\rho = \rho(\vec{\mathbf{y}}, \vec{\mathbf{m}}, \omega). \tag{2.10}$$

This means that the down-ramped data model is more complicated than assumed in equations (2.2) and (2.4) or, equivalently, after discretization, in (2.5)-(2.7). In integral form it is given by

$$d(s, \omega) = \overline{\widehat{f}(\omega)}\widehat{u}(s, \omega)e^{-2i\omega\tau(s, \vec{\mathbf{y}}_o)}$$

$$= k^2|\widehat{f}(\omega)|^2 \int_\Omega d\vec{\mathbf{y}}\, \rho(\vec{\mathbf{y}}, \vec{\mathbf{m}}(s, \vec{\mathbf{y}}), \omega) \frac{\exp\left[2i\omega\big[\tau(s, \vec{\mathbf{y}}) - \tau(s, \vec{\mathbf{y}}_o)\big]\right]}{\big(4\pi|\vec{\mathbf{r}}(s) - \vec{\mathbf{y}}|\big)^2}, \tag{2.11}$$

where $\vec{\mathbf{m}}(s, \vec{\mathbf{y}})$ is the unit vector pointing from the platform location $\vec{\mathbf{r}}(s)$ to $\vec{\mathbf{y}}$ in the image window $\mathcal{Y}$. In discretized form we still have a linear system like (2.6), except that now $\boldsymbol{\rho}$ is a vector of QN_sN_ω unknowns, the discretized values of ρ in the image window $\mathcal{Y}$.

Extending the inversion approaches described in the previous section to this model means inverting approximately the matrix $\mathbf{A}$ with a very large number of columns. We cannot expect the migration formula (1.1) to give an accurate estimate of the reflectivity as a function of five variables, as pointed out in the introduction. The ℓ_1 optimization approach works, but it becomes impractical for the large number QN_sN_ω of unknowns. Moreover, it does not take into account the fact that the entries in $\boldsymbol{\rho}$ indexed by the slow time and frequency pairs (j, l), with $j = 1, \ldots, N_s$ and $l = 1, \ldots, N_\omega$, refer to the same locations $\vec{\mathbf{y}}_q$ on the imaging grid.

The imaging approach introduced in this paper gives an efficient way of estimating direction and frequency dependent reflectivity functions of strong localized scatterers in $\mathcal{Y}$. It uses an approximation of the model (2.11), motivated by the expectation that the backscatter reflectivity should not change dramatically from one platform location to the next and from one frequency to another. Instead of discretizing ρ over all five variables at once, we discretize it only with respect to the location in the image window $\mathcal{Y}$, for one probing direction and frequency at a time. To do so, we separate the data over subsets defined by carefully callibrated sub-apertures and sub-bands, and freeze the direction and frequency dependence of the reflectivity for each subset. The grand optimization is divided this way into smaller optimizations for Q unknowns, which are then coupled by requiring that the unknown vectors share the same spatial support in the imaging window $\mathcal{Y}$.

3. Reduction to the Multiple Measurement Vector framework. We present here an analysis of how we can write the linear relation between the direction and frequency dependent reflectivity and the data as a linear matrix system

$$\mathbb{A}\mathbf{X} = \mathbf{D}, \tag{3.1}$$

where the unknown is the matrix $\mathbf{X}$ with Q rows. The entries in the rows correspond to the discretization of this reflectivity at the Q grid points $\vec{\mathbf{y}}_q$ in $\mathcal{Y}$. Each column of $\mathbf{X}$ depends on the reflectivity at the backscattered direction defined by the center of a sub-aperture and the center frequency of a sub-band. The data are segmented over $\mathcal{N}_\alpha$ sub-apertures and $\mathcal{N}_\beta$ sub-bands and are grouped in the matrix $\mathbf{D}$. The objective of this section is to describe the data segmentation and derive the linear system (3.1), which can be inverted with the MMV approach as explained in section 4.

We begin in section 3.2 with a single sub-aperture and sub-band. We show in Lemma 3.1 that with proper calibration of the sub-aperture and sub-band size, the reflectivity-to-data matrix has a simple approximate form. Its entries have nearly constant amplitudes while the phases depend linearly on the slow time and frequency parametrizing the data subset. This simplification allows us to transform the linear system via coordinate rotation to a reference one, for all data subsets, as shown in section 3.3. The matrix $\mathbb{A}$ in (3.1) corresponds to the reference sub-aperture and sub-band, and the statement of the result is in Proposition 3.2.

3.1. The sub-aperture and sub-band segmentation. We enumerate the sub-apertures by $\alpha = 1, \ldots, \mathcal{N}_\alpha$, and denote by $s_\alpha^\star$ the slow time that corresponds to their center location $\vec{\mathbf{r}}(s_\alpha^\star)$. The choice of the sub-aperture size a is important, and we address it in the next section. For now it suffices to say that it is small enough so that we can approximate it by a line segment, as illustrated in Figure 3.1. The unit tangent vector along the trajectory, at the center of the sub-aperture, is denoted by $\vec{\mathbf{t}}_\alpha$, and the platform motion will be assumed uniform, at speed $V\vec{\mathbf{t}}_\alpha$. The unit vector from the reference location $\vec{\mathbf{y}}_o$ in the image window to $\vec{\mathbf{r}}(s_\alpha^\star)$ is $\vec{\mathbf{m}}_\alpha$. We call it the range vector for the α sub-aperture. The range (distance) to the imaging window is

$$L_\alpha = |\vec{\mathbf{r}}(s_\alpha^\star) - \vec{\mathbf{y}}_o|. \tag{3.2}$$

Each sub-aperture is parametrized by the slow time offset from $s_\alpha^\star$, denoted by

$$\Delta s = s - s_\alpha^\star \in \Big[-\frac{a}{2V}, \frac{a}{2V} \Big]. \tag{3.3}$$

We do not index it by α because it belongs to the same interval for each sub-aperture. The discretization of Δs is at the slow time sample spacing h_s, and there are

$$n_s = \frac{a}{V h_s} + 1$$

sample points, where $a/(V h_s)$ is rounded to an integer. Similarly, we divide the bandwidth in $\mathcal{N}_\beta$ sub-bands of support $b \leq B$, centered at $\omega_\beta^\star$, and let $\Delta\omega$ be the frequency offset

$$\Delta\omega = \omega - \omega_\beta^\star \in \Big[-\pi b, \pi b \Big]. \tag{3.4}$$

We sample the sub-band with n_ω points.

The reflectivity dependence on the direction and frequency is denoted by the superscript pair (α, β), and by discretizing it with the Q points in $\mathcal{Y}$ we obtain the vector of unknowns $\boldsymbol{\rho}^{(\alpha,\beta)} \in \mathbb{C}^Q$. It is mapped to the data vector $\mathbf{d}^{(\alpha,\beta)}$ with entries given by the samples of $d(s_\alpha^\star + \Delta s, \omega_\beta^\star + \Delta\omega)$. The mapping is via the $n_s n_\omega \times Q$ reflectivity-to-data matrix $\mathbf{A}^{(\alpha,\beta)}$ described in Lemma 3.1.

3.2. Reflectivity-to-data model for a single sub-aperture and sub-band. Here we explain how we can choose the size of the sub-apertures and frequency sub-bands so that we can simplify the reflectivity-to-data matrix. The calibration depends on the size of the imaging window $\mathcal{Y}$, which is quantified with two length scales

$$Y_\alpha = \max_{q=1,\ldots Q} |(\vec{\mathbf{y}}_q - \vec{\mathbf{y}}_o) \cdot \vec{\mathbf{m}}_\alpha|, \tag{3.5}$$

and

$$Y_\alpha^\perp = \max_{q=1,\ldots Q} |\mathbb{P}_\alpha(\vec{\mathbf{y}}_q - \vec{\mathbf{y}}_o)|. \tag{3.6}$$

6

Here $\mathbb{P}_\alpha = I - \vec{\mathbf{m}}_\alpha \vec{\mathbf{m}}_\alpha^T$ is the projection on the cross-range plane orthogonal to $\vec{\mathbf{m}}_\alpha$, and I is the identity matrix. The length scale Y_α gives the size of $\mathcal{Y}$ viewed from the range direction $\vec{\mathbf{m}}_\alpha$, and $Y_\alpha^\perp$ is the cross-range size.

The first constraints on the aperture a and the cross-range size $Y_\alpha^\perp$ of the imaging window state that they are not too small, and thus imaging with adequate resolution can be done with the data subset. Explicitly, we ask that for all $\alpha = 1, \ldots, \mathcal{N}_\alpha$,

$$\frac{a^2}{\lambda_o L_\alpha} \gtrsim \frac{a Y_\alpha^\perp}{\lambda_o L_\alpha} \gtrsim \frac{(Y_\alpha^\perp)^2}{\lambda_o L_\alpha} \gtrsim 1. \tag{3.7}$$

The inequalities on the left involve two Fresnel numbers $a^2/(\lambda_o L_\alpha)$ and $(Y_\alpha^\perp)^2/(\lambda_o L_\alpha)$, whose magnitude define the imaging regime. If these numbers were small, we would be in a Fraunhoffer diffraction regime, with approximately planar wavefronts on the scale of the sub-aperture and of the size of the imaging window. We consider a Fresnel diffraction regime, where these numbers are larger and we can get better resolution of images. The cross-range resolution is $\lambda_o L_\alpha/a$, and naturally, the middle inequality in (3.7) says that the image window is larger than the resolution limit. In the range direction we suppose that

$$Y_\alpha \gtrsim \frac{c}{b} \gg \lambda_o, \tag{3.8}$$

where c/b is the range resolution for the sub-bands, and we used that $b \leq B \ll \omega_o$.

While we would like to have a and b large so as to get good spatial resolution of the unknown reflectivity, we recall that ρ is frozen in our discretization in the small frequency sub-band and in the narrow cone of opening angle of the order a/L_α, with axis defined by the center $\vec{\mathbf{r}}(s_\alpha^\star)$ of the sub-aperture and the reference point $\vec{\mathbf{y}}_o$. The larger a and b are, the coarser the estimation of the direction and frequency dependence of ρ. The more rapid the variation of ρ with direction and frequency, the smaller a and b should be to represent it, at the expense of resolution.

There is also a trade-off between resolution and the complexity of the inversion algorithm. By constraining a and b so that

$$\frac{b}{\omega_o} \frac{Y_\alpha^\perp}{\lambda_o L_\alpha/a} \ll 1, \tag{3.9}$$

and

$$\frac{a^2 Y_\alpha}{\lambda_o L_\alpha^2} \ll 1, \qquad \frac{a^2 Y_\alpha^\perp}{\lambda_o L_\alpha^2} \ll 1, \tag{3.10}$$

we can simplify the mapping between the reflectivity and the data subset, as stated in Lemma 3.1. This simplification allows us to use the efficient MMV framework to solve the large optimization problem for the entire data set, by considering jointly the smaller problems for the segmented data in an automatic way. The key observation here is that the unknown reflectivities for each data subset share the same spatial support. This is what the MMV formalism is designed to capture.

The next lemma gives the form of the reflectivity-to-data matrix in the linear system

$$\mathbf{A}^{(\alpha,\beta)} \boldsymbol{\rho}^{\alpha,\beta} = \mathbf{d}^{(\alpha,\beta)}, \tag{3.11}$$

for the (α, β) data subset. It is an approximation of the system (2.6) restricted to the rows indexed by the n_s slow times in the $\alpha-$aperture and the n_ω frequencies in the $\beta-$band. The expression of $\mathbf{A}^{(\alpha,\beta)}$ is derived in appendix A.

LEMMA 3.1. *Under the assumptions (3.7)-(3.10), and with the pulse model (2.3), the matrix $\mathbf{A}^{(\alpha,\beta)}$ consists of n_ω blocks $\mathbf{A}^{(\alpha,\beta)}(\Delta\omega_l)$ indexed by the frequency offset $\Delta\omega_l$, for $l = 1, \ldots, n_\omega$. Each block is an $n_s \times Q$ matrix with entries defined by*

$$A_{j,q}^{(\alpha,\beta)}(\Delta\omega_l) = \frac{k_o^2 |\widehat{f}(\omega_o)|^2}{(4\pi L_\alpha)^2} \exp\left\{ -2i(k_\beta + \Delta\omega_l/c)\vec{\mathbf{m}}_\alpha \cdot \vec{\mathbf{y}}_q \right.$$
$$\left. -2ik_\beta V \Delta s_j \frac{\vec{\mathbf{t}}_\alpha \cdot \mathbb{P}_\alpha \Delta\vec{\mathbf{y}}_q}{L_\alpha} + ik_\beta \frac{\Delta\vec{\mathbf{y}}_q \cdot \mathbb{P}_\alpha \Delta\vec{\mathbf{y}}_q}{L_\alpha} \right\}, \tag{3.12}$$

where $k_\beta = \omega_\beta^\star/c$, and $\Delta\vec{\mathbf{y}}_q = \vec{\mathbf{y}}_q - \vec{\mathbf{y}}_o$.

3.3. Multiple sub-aperture and sub-band model as an MMV system. It remains to show how to write equations (3.11) in the matrix form (3.1) with a reflectivity-to-data matrix independent of the sub-apertures and sub-bands. This is accomplished via a rotation, that brings all the sub-apertures to a single reference sub-aperture. But to do this, we need to know that each data subset has a similar view of the image window. Mathematically, this is expressed by the following two additional constraints on a and b

$$\max_{1\leq \alpha \leq \mathcal{N}_\alpha, 1\leq q\leq Q} \frac{b}{c}\left|(\vec{\mathbf{m}}_\alpha - \vec{\mathbf{m}}_1)\cdot \Delta\vec{\mathbf{y}}_q\right| \ll 1, \tag{3.13}$$

and

$$\max_{1\leq \alpha \leq \mathcal{N}_\alpha, 1\leq \beta \leq \mathcal{N}_\beta, 1\leq q\leq Q}\left|\left(\frac{ak_\beta}{L_\alpha}\vec{\mathbf{t}}_\alpha \cdot \mathbb{P}_\alpha - \frac{ak_1}{L_1}\vec{\mathbf{t}}_1 \cdot \mathbb{P}_1\right)\Delta\vec{\mathbf{y}}_q\right| \ll 1, \tag{3.14}$$

The constraint (3.13) states that the imaging points remain within the range resolution limit b/c for all the apertures. The constraint (3.14) states that the imaging points remain within the cross-range resolution limits, as well.

The derivation of the linear system (3.1) is in appendix A and the result is stated in the next proposition.

PROPOSITION 3.2. *Under the same assumption as in Lemma 3.1 and in addition, supposing that conditions (3.13) and (3.14) hold, we can combine the linear systems (3.11) in the matrix equation (3.1). The reference sub-aperture and sub-band are indexed by $\alpha = 1$ and $\beta = 1$. The unknown matrix $\mathbf{X}$ has Q rows and $\mathcal{N}_\alpha \mathcal{N}_\beta$ columns indexed by (α, β). Its entries are*

$$X_q^{(\alpha,\beta)} = \rho_q^{(\alpha,\beta)} \exp\left[-2ik_\beta \vec{\mathbf{m}}_\alpha \cdot \Delta\vec{\mathbf{y}}_q + ik_\beta \frac{\Delta\vec{\mathbf{y}}_q \cdot \mathbb{P}_\alpha \Delta\vec{\mathbf{y}}_q}{L_\alpha}\right], \tag{3.15}$$

where

$$\rho_q^{(\alpha,\beta)} = \rho(\vec{\mathbf{y}}_q, \vec{\mathbf{m}}_\alpha, \omega_\beta^\star), \qquad \vec{\mathbf{m}}_\alpha = \frac{\vec{\mathbf{r}}(s_\alpha^\star) - \vec{\mathbf{y}}_o}{|\vec{\mathbf{r}}(s_\alpha^\star) - \vec{\mathbf{y}}_o|}. \tag{3.16}$$

The data matrix $\mathbf{D}$ has $n_s n_\omega$ rows and $\mathcal{N}_\alpha \mathcal{N}_\beta$ columns indexed by (α, β). We organize the equations in blocks indexed by the frequency $\Delta\omega_l$, for $l = 1, \ldots, n_\omega$. The entries of $\mathbf{D}$ are defined in terms of the down-ramped data vectors $\mathbf{d}^{(\alpha,\beta)}$ as

$$D_j^{(\alpha,\beta)}(\Delta\omega_l) = \frac{(4\pi L_\alpha)^2}{k_o^2|\widehat{f}(\omega_o)|^2} d^{(\alpha,\beta)}(\Delta s_j, \Delta\omega_l), \tag{3.17}$$

where we recall that

$$d^{(\alpha,\beta)}(\Delta s_j, \Delta\omega_l) = d\left(s_\alpha^\star + \Delta s_j, \omega_\beta^\star + \Delta\omega_l\right), \tag{3.18}$$

and $d(s, \omega)$ is defined in (2.5). The reflectivity to data matrix $\mathbb{A}$ has n_ω blocks indexed by $\Delta\omega_l$, denoted by $\mathbb{A}(\Delta\omega_l)$. Each block is an $n_s \times Q$ matrix with entries

$$\mathbb{A}_{j,q}(\Delta\omega_l) = \exp\left[-2i\frac{\Delta\omega_l}{c}\vec{\mathbf{m}}_1 \cdot \Delta\vec{\mathbf{y}}_q - 2ik_1\frac{V\Delta s_j}{L_1}\vec{\mathbf{t}}_1 \cdot \mathbb{P}_1 \Delta\vec{\mathbf{y}}_q\right]. \tag{3.19}$$

Note that the product of the reflectivity-to-data matrix $\mathbb{A}$ with each column of $\mathbf{X}$ can be interpreted, up to a constant multiplicative factor, as a Fourier transform with respect to the range offset $\vec{\mathbf{m}}_1 \cdot \Delta\vec{\mathbf{y}}$ and cross-range offset $\vec{\mathbf{t}}_1 \cdot \mathbb{P}_1 \Delta\vec{\mathbf{y}}$ in $\mathcal{Y}$. Equation (3.15) shows that the columns of $\mathbf{X}$ differ from each other by a linear phase factor in $\Delta\vec{\mathbf{y}}$, which amounts to a rotation of the coordinate system of the α sub-aperture, and a quadratic factor which corrects for Fresnel diffraction effects. Thus, the linear system (3.1) gives roughly the Fourier transform of the reflectivity ρ for different range direction views, and the imaging problem is to invert it to estimate ρ.

4. Inversion algorithm. Here we describe the algorithm that estimates the reflectivity by inverting the linear system (3.1). By construction, the columns of the $Q \times \mathcal{N}_\alpha \mathcal{N}_\beta$ unknown matrix $\mathbf{X}$ have the same spatial support, because they represent the same spatial reflectivity function. Thus, we formulate the inversion as a common support recovery problem for unknown matrices with relatively few nonzero rows [19, 6, 9, 12]. This Multiple Measurement Vector (MMV) formulation has been studied in [12, 6, 19] and has been used successfully

for source localization with passive arrays of sensors in [16] and for imaging strong scattering scenes, where multiple scattering effects cannot be neglected, in [5].

In the MMV framework the support of the unknown matrix $\mathbf{X}$ is quantified by the number of nonzero rows, that is the row-wise ℓ_0 norm of $\mathbf{X}$. If we define the set

$$\text{rowsupp}(\mathbf{X}) = \{q = 1, \ldots, Q \ \text{ s.t. } \ \|\mathbf{e}_q^T \mathbf{X}\|_{\ell_2} \neq 0\}, \tag{4.1}$$

where $\mathbf{e}_q^T \mathbf{X}$ is the q−th row of $\mathbf{X}$ and $\mathbf{e}_q$ is the vector with entry 1 in the q−th row and zeros elsewhere, then the row-wise ℓ_0 norm of $\mathbf{X}$ is the cardinality of $\text{rowsupp}(\mathbf{X})$,

$$\Xi_0(\mathbf{X}) = |\text{rowsupp}(\mathbf{X})|.$$

To estimate $\mathbf{X}$ we must to solve the optimization problem

$$\min \Xi_0(\mathbf{X}) \quad \text{s.t.} \quad \mathbb{A}\mathbf{X} = \mathbf{D}, \tag{4.2}$$

but this is an NP hard problem. We solve instead the convex problem

$$\min J_{2,1}(\mathbf{X}) \quad \text{s.t.} \quad \mathbb{A}\mathbf{X} = \mathbf{D}, \tag{4.3}$$

which gives, under certain conditions on the model matrix $\mathbb{A}$ [12, 5], the same solution as (4.2). In (4.3) $J_{2,1}$ denotes the $(2,1)$-norm

$$J_{2,1}(\mathbf{X}) = \sum_{q=1}^{m} \|\mathbf{e}_q^T \mathbf{X}\|_{\ell_2}, \tag{4.4}$$

which is the ℓ_1 norm of the vector formed by the ℓ_2 norms of the rows of $\mathbf{X}$. Furthermore, because data are noisy in practice, we replace the equality constraint in (4.3) by $\|\mathbb{A}\mathbf{X} - \mathbf{D}\|_F < \epsilon$, where $\|\cdot\|_F$ is the Frobenius norm and ϵ is a tolerance commensurate with the noise level of the data.

There are different algorithms for solving (4.3) or its reformulation for noisy data. We use an extension of an iterative shrinkage-thresholding algorithm, called GeLMA, proposed in [17] for matrix-vector equations. This algorithm is very efficient for solving ℓ_1-minimization problems, and has the advantage that the solution does not depend on the regularization parameter used to promote minimal support solutions, see [17] for details.

Algorithm 1 GeLMA-MMV

Require: Set $\mathbf{X} = \mathbf{0}$, $\boldsymbol{\mathcal{Z}} = \mathbf{0}$, and pick the step size μ and the regularization parameter γ.
  repeat
    Compute the residual $\boldsymbol{\mathcal{E}} = \mathbf{D} - \mathbb{A}\mathbf{X}$
    $\mathbf{X} \Leftarrow \mathbf{X} + \mu \mathbf{A}^*(\boldsymbol{\mathcal{Z}} + \boldsymbol{\mathcal{E}})$
    $\mathbf{e}_q^T \mathbf{X} \Leftarrow \text{sign}(\|\mathbf{e}_q^T \mathbf{X}\|_{\ell_2} - \mu\gamma)\frac{\|\mathbf{e}_q^T \mathbf{X}\|_{\ell_2} - \mu\gamma}{\|\mathbf{e}_q^T \mathbf{X}\|_{\ell_2}}\mathbf{e}_q^T \mathbf{X}, \quad q = 1, \ldots, Q$
    $\boldsymbol{\mathcal{Z}} \Leftarrow \boldsymbol{\mathcal{Z}} + \gamma\boldsymbol{\mathcal{E}}$
  until Convergence

After estimating $\mathbf{X}$ with Algorithm 1, we recover the discretized direction and frequency dependent reflectivity using equation (3.15),

$$\rho_q^{(\alpha,\beta)} = X_q^{(\alpha,\beta)} \exp\left[2ik_\beta \vec{\mathbf{m}}_\alpha \cdot \Delta\vec{\mathbf{y}}_q - ik_\beta \frac{\Delta\vec{\mathbf{y}}_q \cdot \mathbb{P}_\alpha \Delta\vec{\mathbf{y}}_q}{L_\alpha}\right], \tag{4.5}$$

for the imaging points $\vec{\mathbf{y}}_q = \vec{\mathbf{y}}_o + \Delta\vec{\mathbf{y}}_q$ indexed by $q = 1, \ldots, Q$, the sub-apertures indexed by $\alpha = 1, \ldots, \mathcal{N}_\alpha$ and frequency sub-bands indexed by $\beta = 1, \ldots, \mathcal{N}_\beta$.

5. Numerical simulations. We begin in section 5.1 with the numerical setup, which is in the regime of the GOTCHA Volumetric data set [3] for X-band persistent surveillance SAR. Then we present in sections 5.2 and 5.3 the simulation results.

5.1. Imaging in the X-band (GOTCHA) SAR regime. The numerical simulations generate the data with the model (2.2), for various scattering scenes. The regime of parameters is that of the GOTCHA data set, where the platform trajectory is circular at height $H = 7.3$km, with radius $R = 7.1$km and speed $V = 70$m/s. The signal $f(t)$ is sent every 1.05m along the trajectory, which gives a slow time spacing $h_s = 0.015$s. The carrier frequency is $\omega_o/(2\pi) = 9.6$GHz and the bandwidth is $B = 622$MHz. The waves propagate at electromagnetic speed $c = 3 \cdot 10^8$m/s, so the wavelength is $\lambda_o = 3.12$cm. The image window $\mathcal{Y}$ is at the ground level, below the center of the flight trajectory, and the distance from the platform to its center $\vec{y}_o$ is $L = 10.18$km. It is a square, with side length $Y = Y^\perp$ of the order of 40m. The size of the sub-apertures is $a = 42$m and the width of each sub-band is $b = B/15$.

Given these parameters, the nominal resolution limits are

$$\lambda_o L/a = 7.56\text{m}, \qquad c/b = 7.23\text{m}.$$

The image window $\mathcal{Y}$ is discretized in uniform steps $h = 2$m in range and $h^\perp = 1$m in cross-range, and the reflectivity is modeled as piecewise constant on the imaging grid. The image discretization affects the quality of the reconstruction with ℓ_1 optimization. It must be coarse enough so that uniqueness of the ℓ_1 minimizer holds, and yet fine enough so that modeling errors due to off-grid placement of the unknown are controlled. We refer to [2] for a study of this trade-off.

To illustrate the performance of the algorithm, we present in the next two sections results for various imaging scenes consisting of small scatterers supported on one pixel of the imaging grid, or over multiple adjacent pixels. The latter is for representing larger scatterers for which the direction dependent reflectivity can be motivated by Snell's law of reflection at their surface.

The results presented in the next sections compare the images obtained with reverse time migration and the algorithm proposed in this paper, hereby referred to as the MMV algorithm. The migration image is computed with the formula

$$\mathcal{I}(\vec{y}) = \frac{(4\pi)^2}{k_o^2 |\widehat{f}(\omega_o)|^2 n_s n_\omega h h^\perp} \sum_{j=1}^{n_s} \sum_{l=1}^{n_\omega} d(s_j, \omega_l) |\vec{r}(s_j) - \vec{y}|^2 e^{-2i\omega_l \left[\tau(s_j, \vec{y}) - \tau(s_j, \vec{y}_o)\right]}, \tag{5.1}$$

which is a weighted version of (1.1), where the weights are chosen so as to provide a quantitative estimate of the unknown ρ. That is to say, when we substitute the data model in (5.1), under the assumption of an isotropic and frequency independent reflectivity we get that $\mathcal{I}(\vec{y})$ peaks at the true location of the scatterers and its value at the peaks equals the true reflectivity there.

Let us verify the assumptions (3.7)-(3.10) with the GOTCHA parameters. The Fresnel numbers are larger than one, as stated in (3.7),

$$\frac{a^2}{\lambda_o L} = 5.55 \quad \text{and} \quad \frac{(Y^\perp)^2}{\lambda_o L} = 5.04.$$

The size of the imaging region and the range resolution satisfy (3.8). Moreover,

$$\frac{b}{\omega_o} \frac{Y^\perp}{\lambda_o L/a} = 0.0036,$$

which is consistent with (3.9), and (3.10) is satisfied as well,

$$\frac{a^2 Y^\perp}{\lambda_o L^2} = \frac{a^2 Y}{\lambda_o L^2} = 0.022.$$

5.2. Single frequency results. We begin with imaging results at the carrier frequency, where we assume we know the range of the scatterers and seek to reconstruct their reflectivity as a function of cross-range and direction. The image window extends over 120m in cross-range, and it is sampled in steps $h^\perp = 1$m, where we recall that $\lambda_o L/a = 7.56$m.

The first result displayed in Figure 5.1 is for an isotropic, frequency independent reflectivity of 11 scatterers, $\mathcal{N}_\alpha = 8$ consecutive, non-overlapping apertures and noiseless data. We display in green the true reflectivity, in blue the reflectivity estimated with formula (5.1), and with broken line the result of the MMV inversion algorithm. In the legend we abbreviate the migration formula result with the letters KM, standing for Kirchhoff Migration.
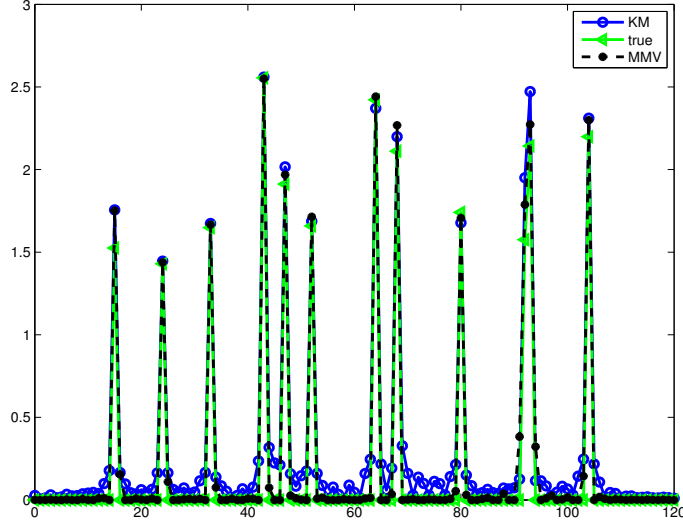
FIG. 5.1. *Estimation of an isotropic, frequency independent reflectivity as a function of cross-range, using $N_\alpha = 8$ consecutive, non-overlapping apertures. The exact reflectivity is shown with the full green line, the migration result with the blue line and the MMV inversion result with the broken line. The abscissa is cross-range in meters.*
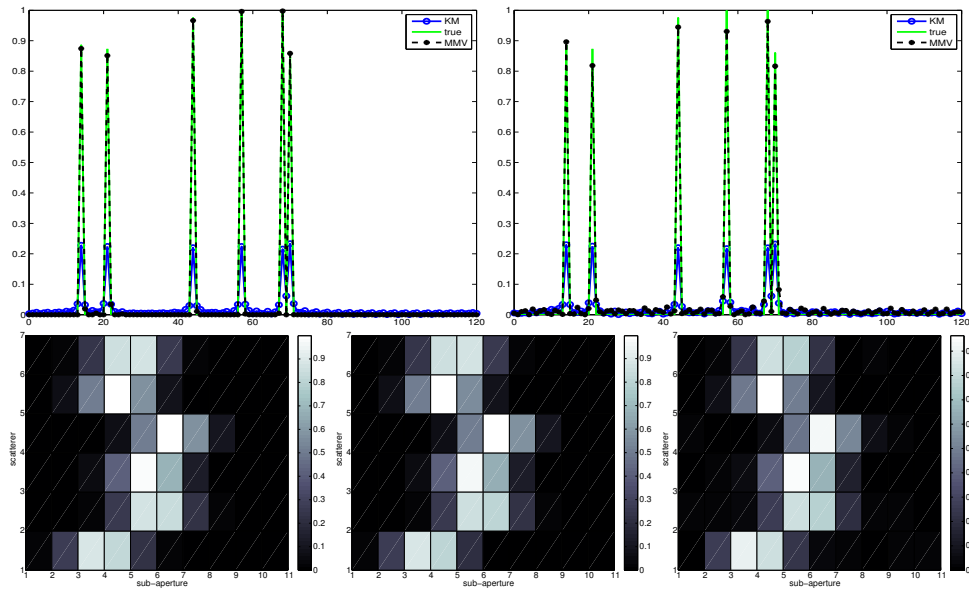

FIG. 5.2. *Estimation of the reflectivity as a function of direction and cross-range location for a scene with 6 scatterers. The top plots show the reflectivity as a function of cross-range (the abscissa in meters), for the peak directions. The left plot is for noiseless data and the right plot is for data contaminated with 10% additive noise. The green line is the exact peak value and the broken line the one obtained with MMV. The blue line is obtained with migration. The bottom plots display the reflectivity of each scatterer as a function of sub-aperture i.e., the slow time index $\alpha = 1, \ldots, 10$, where 10 is the number of sub-apertures. The left plot is for the true reflectivity, the middle plot is for the noiseless reconstruction and the right plot is for the noisy reconstruction.*

The figure shows that the MMV algorithm reconstructs exactly the reflectivity, and that the weighted migration formula (5.1) does indeed give quantitative estimates of the reflectivity. However, the migration estimates deteriorate when the reflectivity is anisotropic and frequency dependent, as illustrated next.

The results displayed in Figure 5.2 are obtained with $\mathcal{N}_\alpha = 10$ consecutive, non-overlapping apertures. The reflectivity depends on two variables: the cross-range location and the scattering direction, parameterized by the slow time $s_\alpha^\star$, for $\alpha = 1, \ldots, 10$. In discretized form it gives a matrix $\mathcal{R}_{\mathrm{true}}$ with row index corresponding to the pixel location in the image window, and column index corresponding to the sub-aperture. The reconstruction of this matrix is denoted by $\mathcal{R}$. The green and broken lines in the top plots in the figure display the true and reconstructed reflectivity at the peak direction, vs. cross-range. Explicitly, for each pixel in the image i.e., each
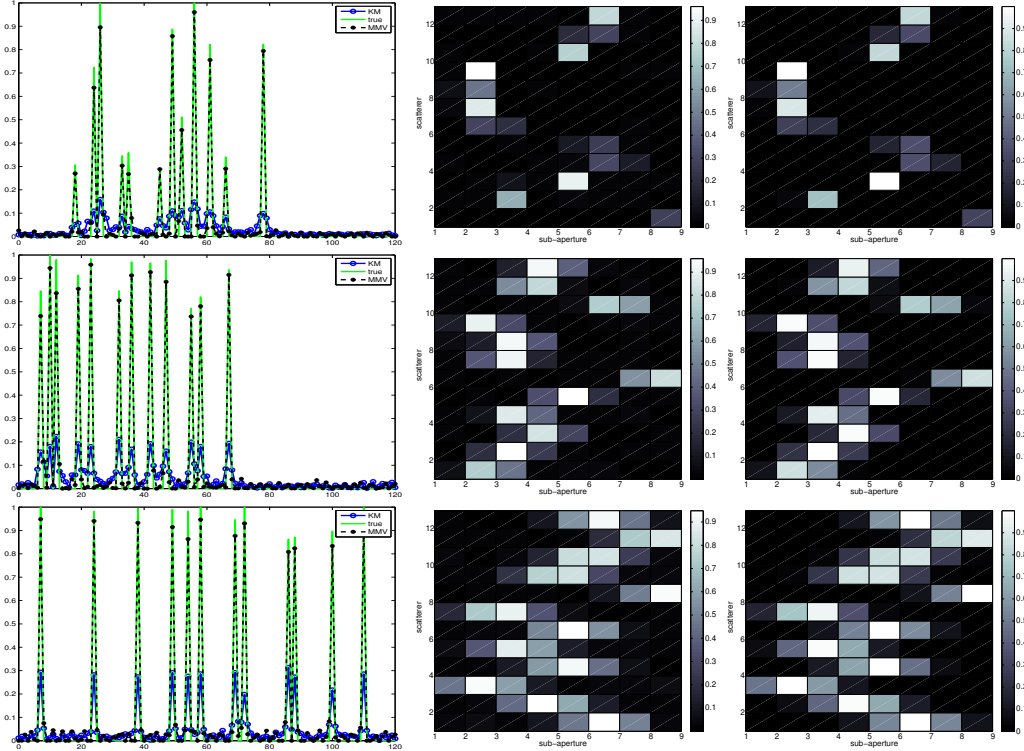
FIG. 5.3. *Imaging results for anisotropic reflectivities, $\mathcal{N}_\alpha = 10$ sub-apertures and data contaminated with 10% additive noise. From top to bottom we decrease the anisotropy. This can be seen from the right column plots which show the reflectivity of each scatterer for each sub-aperture. The middle column shows the reconstructed reflectivity as a function of direction with the MMV algorithm.*

row q in $\mathcal{R}_{\text{true}}$ or $\mathcal{R}$, we display the maximal entry. The migration image of the reflectors is independent of the direction and is plotted with the blue line. The results show that we have 6 small scatterers, which are well estimated by the MMV algorithm even for noisy data. The migration method identifies correctly the locations of the 6 scatterers, but the reflectivity value is no longer accurate because only a few sub-apertures see each reflector, as we infer from the bottom plots described next. This also implies a deterioration in the cross-range resolution which is more visible in the next set of results in Figure 5.3. Naturally, the migration image gives no information about the direction dependence of the reflectivity.

In the bottom plots in Figure 5.2 we show the value of the reflectivity of each scatterer as a function of direction, parameterized by the slow time $s_\alpha^\star$. That is to say, we identify first the row indexes q in $\mathcal{R}_{\text{true}}$ or $\mathcal{R}$ at which we have a strong scatterer (see top plots) and then display those rows. The left plot is for the true reflectivity, the middle is for the noiseless reconstruction, and the right is for the noisy reconstruction. We observe that the MMV method reconstructs the direction dependent reflectivity exactly in the noiseless case, and very well in the noisy case.

In Figure 5.3 we illustrate the effect of the anisotropy of the reflectivity on the imaging process. We display the results the same way as in in the previous figure. The point is to notice that while the MMV method estimates accurately the direction dependent reflectivity in all cases, the migration method performs poorly when the anisotropy is strong, meaning that each scatterer is seen only by one sub-aperture at a time (top plots). The resolution is not that corresponding to the actual aperture of $10a = 420$m, but that for a single sub-aperture of $a = 42$m. The middle and bottom row plots show how migration images improve when the anisotropy of the reflectivity is weaker and more sub-apertures see each scatterer.

5.3. Multiple frequency results. Now we consider multiple frequency sub-bands and thus seek to estimate the reflectivity as a function of range, cross-range, direction and frequency. We have $\mathcal{N}_\omega$ sub-bands of width b, and we sample each of them at $n_\omega = 15$ frequencies. The number of sub-apertures is $\mathcal{N}_\alpha = 8$. The imaging region is a square of side 40m and it is sampled in cross-range in steps $h^\perp = 1$m and in range in steps $h = 2$m. We denote, as before, by $\mathcal{R}_{\text{true}}$ the true matrix of discretized reflectivities and by $\mathcal{R}$ the reconstructed ones. These
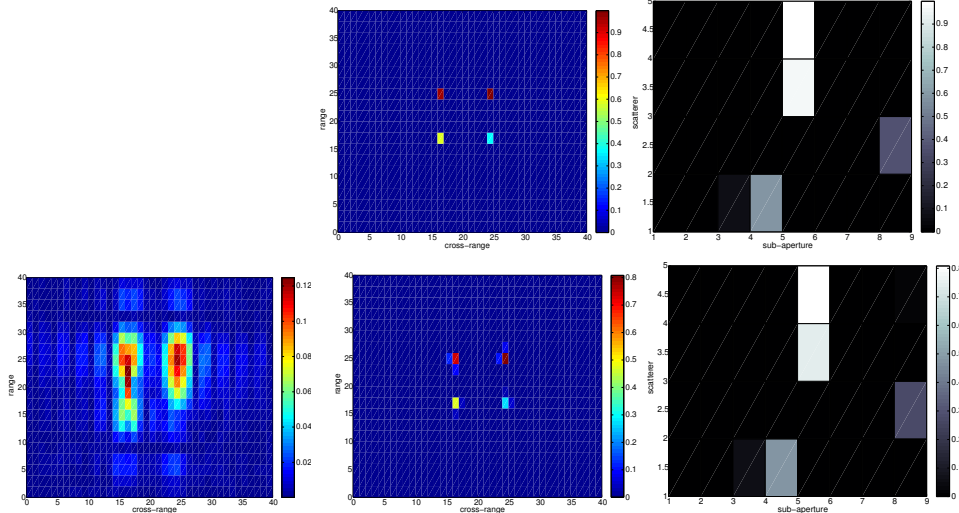
FIG. 5.4. *Results for a single frequency sub-band and $\mathcal{N}_\alpha = 8$ consecutive, non-overlapping sub-apertures. On the top we show the true reflectivity as a function of location (middle) and direction (right). On the bottom we show the reconstructed reflectivity with 20% additive noise. Left plot is the migration image, middle plot is the MMV image and the right plot is the directional dependence of the reflectivity reconstructed with the MMV algorithm. The axes in the left images are cross-range and range in meters. The abscissa in the right plots are sub-aperture index $\alpha = 1, \ldots, \mathcal{N}_\alpha$ and the ordinate is the index of the scatterer (from 1 to 4).*

are matrices of size $Q \times \mathcal{N}_\alpha \mathcal{N}_\omega$ and we display them in the image window $\mathcal{Y}$ as follows: For each pixel in the image window i.e., a row q in $\mathcal{R}_{\text{true}}$ or $\mathcal{R}$, we display the maximum entry, the peak value of the reflectivity at point $\vec{\mathbf{y}}_q$ over directions and frequencies. Once we identify the location of the scatterers from these images, i.e., determine their associated rows, we display the entries in these rows, to illustrate the direction and frequency dependence of their reflectivity. These are the middle and right plots in the figures.

We begin in Figure 5.4 with a single frequency sub-band ($\mathcal{N}_\omega = 1$), $\mathcal{N}_\alpha = 8$ consecutive, non-overlapping sub-apertures and data contaminated with 20% additive noise. The anisotropic reflectivity model has four scatterers, as illustrated in the top plots. Each scatterer is seen by a single sub-aperture. The reconstructed reflectivity is shown in the bottom plots. On the left we show the migration image, which is blurry and is unable to locate the weaker scatterers. The MMV algorithm gives an excellent reconstruction as shown in the middle and right plots.

The results in Figures 5.5 and 5.6 are for $\mathcal{N}_\omega = 8$ consecutive, non-overlapping frequency bands and $\mathcal{N}_\alpha = 8$ consecutive, non-overlapping sub-apertures. The difference between the figures is the strength of the scatterers and their anisotropy. The results in Figure 5.5 show that the MMV algorithm reconstructs well the location of the scatterers and the direction dependence of their reflectivity. The frequency dependence of the weaker scatterers is not that accurate, likely because the bandwidth is small and all frequencies are similar to the carrier. As in Figure 5.4, the migration image is blurrier and does not locate the weak scatterers. Figure 5.6 shows that the migration image improves when all scatterers are of approximately the same strength and they have weaker anisotropy.

The last illustration considers a larger scatterer with direction dependent reflectivity, supported over four adjacent pixels, and a small isotropic scatterer with frequency dependent reflectivity. The data is contaminated with 20% additive noise. We note that the migration method gives the correct location of the large scatterer, but not the value of its reflectivity. Moreover, it gives a blurry image of the small scatterer. The MMV algorithm determines well the support of both scatterers, as well as accurate estimates of the reflectivity as a function of direction and frequency.

6. Doppler effects. All the results up to now use the start-stop approximation of the data model, which neglects the motion of the platform over the fast time recording window. Here we extend them to regimes where Doppler effects are important. We begin in section 6.1 with the derivation of the generalized data model that includes Doppler effects, and an assessment of the validity of the start-stop approximation. Then we explain in section 6.2 how to incorporate these effects in our imaging algorithm.

6.1. Data model with Doppler effects. For simplicity we first derive the data model for an isotropic reflectivity $\rho = \rho(\vec{\mathbf{y}})$. Then we extend it in the obvious way to direction and frequency dependent reflectivities in
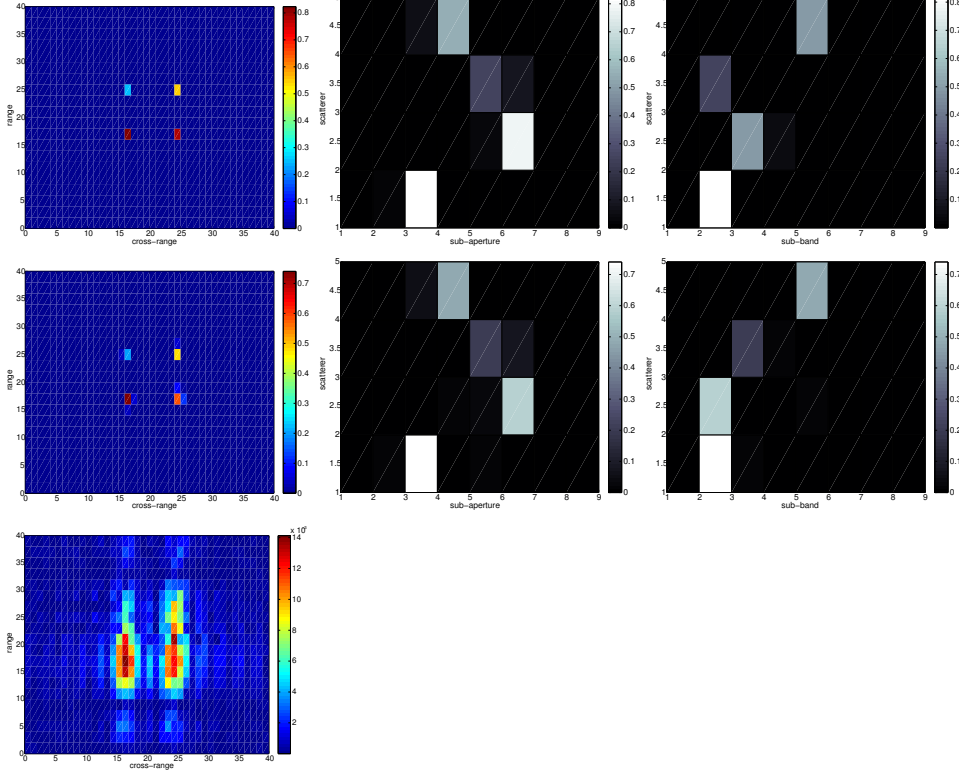
13

Fig. 5.5. *Results with $\mathcal{N}_\omega = 8$ frequency intervals, $\mathcal{N}_\alpha = 8$ apertures and data contaminated with 20% noise. On the top we show the true reflectivity as a function of location (left) and direction (middle), and frequency (right). In the middle row we show the reconstructed reflectivity with the MMV algorithm. The plot in the bottom row is the migration image. The axes in the left images are cross-range and range in meters. The abscissa in the middle and right plots are the sub-aperture and sub-band index and the ordinate is the index of the scatterer (from 1 to 4).*

a sub-aperture indexed by α and sub-band indexed by β, with reflectivity $\rho^{(\alpha,\beta)}(\vec{y})$.

The scattered wave $u(s,t)$ recorded at the transmit-receive platform is given by

$$u(s,t) = -\int_\Omega d\vec{y} \frac{\rho(\vec{y})}{c^2} \int_0^t dt_1 \int_0^{t_1} dt_2\, f''(t_2) G(t_1 - t_2, \vec{r}(s+t_2), \vec{y}) G(t - t_1, \vec{y}, \vec{r}(s+t)),$$

$$= -\frac{1}{c^2} \int_\Omega d\vec{y} \rho(\vec{y}) \frac{f''(t_2(t))}{(4\pi)^2 |\vec{r}(s+t_2(t)) - \vec{y}||\vec{r}(s+t) - \vec{y}|} \tag{6.1}$$

where $t_2(t)$ is the solution of the equation

$$t_2 + \frac{|\vec{r}(s+t_2) - \vec{y}|}{c} = t - \frac{|\vec{r}(s+t) - \vec{y}|}{c}, \tag{6.2}$$

and we used the expression of the Green's function of the wave equation

$$G(t, \vec{r}, \vec{y}) = \frac{\delta\big[t - |\vec{r} - \vec{y}|/c\big]}{4\pi |\vec{r} - \vec{y}|},$$

and the single scattering approximation. The expression (6.1) is simply the spherical wave emitted from $\vec{r}(s+t_2)$, over the duration t_2 of the pulse, scattered isotropically at $\vec{y}$, and then recorded at $\vec{r}(t+s)$. Up to the single scattering approximation, this is an exact formula. Expanding with respect to t the arguments in (6.1) and (6.2) we obtain

$$u(s,t) = -\frac{1}{c^2} \int_\Omega d\vec{y} \rho(\vec{y}) \frac{1}{(4\pi |\vec{r}(s) - \vec{y}|)^2 \big(1 + O(Vt/L)\big)} \times$$

$$f'' \Big[\Big(t\Big(1 - \gamma(s,\vec{y}) + O\Big(\frac{V}{c}\frac{Vt}{R}\Big)\Big) - 2\tau(s,\vec{y}) \Big) / \Big(1 + \gamma(s,\vec{y}) + O\Big(\frac{V}{c}\frac{Vt}{R}\Big) \Big) \Big], \tag{6.3}$$
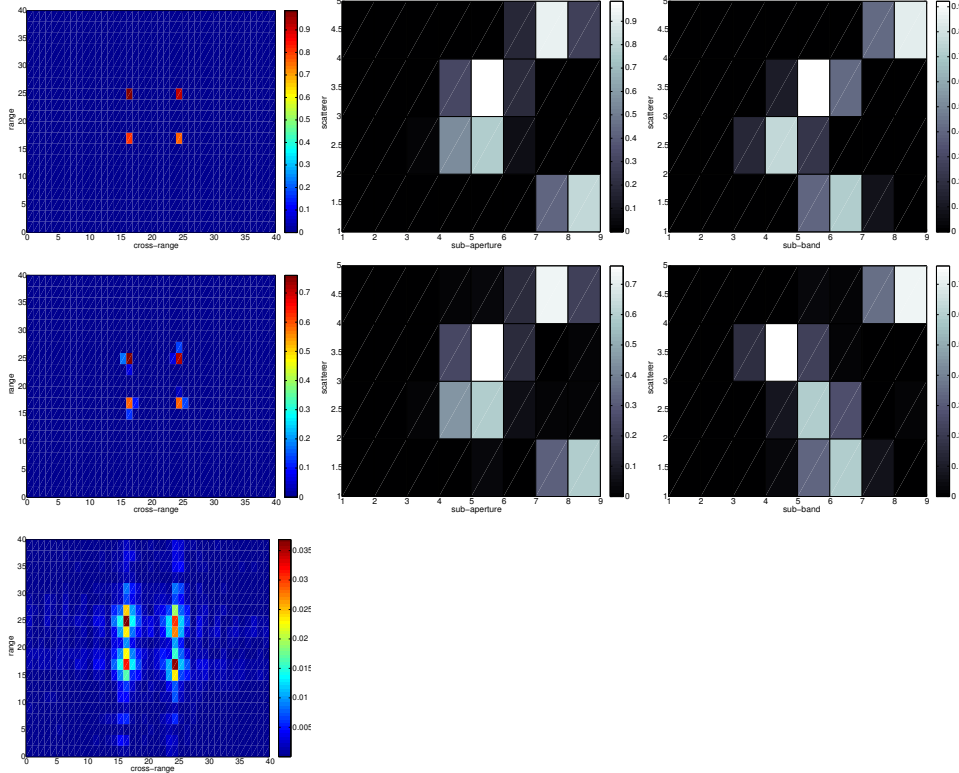
14

FIG. 5.6. *Results with $\mathcal{N}_\omega = 8$ frequency intervals, $\mathcal{N}_\alpha = 8$ apertures and data contaminated with 20% noise. On the top we show the true reflectivity as a function of location (left), direction (middle), and frequency (right). In the middle row we show the reconstructed reflectivity with the MMV algorithm. The plot in the bottom row is the migration image. The axes in the left images are cross-range and range in meters. The abscissa in the middle and right plots are the sub-aperture and sub-band index and the ordinate is the index of the scatterer.*

where we introduced the Doppler factor γ defined by

$$\gamma(s, \vec{y}) = \frac{\vec{r}'(s)}{c} \cdot \vec{m}(s, \vec{y}), \qquad \vec{m}(s, \vec{y}) = \frac{\vec{r}(s) - \vec{y}}{|\vec{r}(s) - \vec{r}(y)|}. \tag{6.4}$$

We assume that the platform is moving at constant speed V along a trajectory with unit tangent denoted by $\vec{t}(s)$, and with radius of curvature R assumed comparable to the range L. Thus,

$$\gamma(s, \vec{y}) = O\left(\frac{V}{c}\right) \ll 1,$$

because the platform speed is typically much smaller than c, the wave speed, and we can neglect the residual in (6.3) which is even smaller than γ, because over the duration of the fast time window the platform travels a small distance compared with the radius of curvature $Vt \ll R \sim L$. We have thus the data model

$$u(s, t) \approx -\frac{1}{c^2} \int_\Omega d\vec{y} \rho(\vec{y}) \frac{f''\left[t\left(1 - 2\gamma(s, \vec{y})\right) - 2\tau(s, \vec{y})\left(1 - \gamma(s, \vec{y})\right)\right]}{(4\pi|\vec{r}(s) - \vec{y}|)^2}, \tag{6.5}$$

which includes first order Doppler effects.

The start-stop approximation is valid when the Doppler factor in the argument of f'' in (6.5) is negligible. Altough γ is small, f'' oscillates at the carrier frequency ω_o which is large and, depending on the scale of the fast time t, the Doppler factor may play a role. Recall that t is limited by the slow time spacing h_s. In practice the duration of the fast time window may be much smaller than h_s, although it must be large enough so that the platform can receive the echoes delayed by the travel time, $2\tau(s, \vec{y})$. Explicitly,
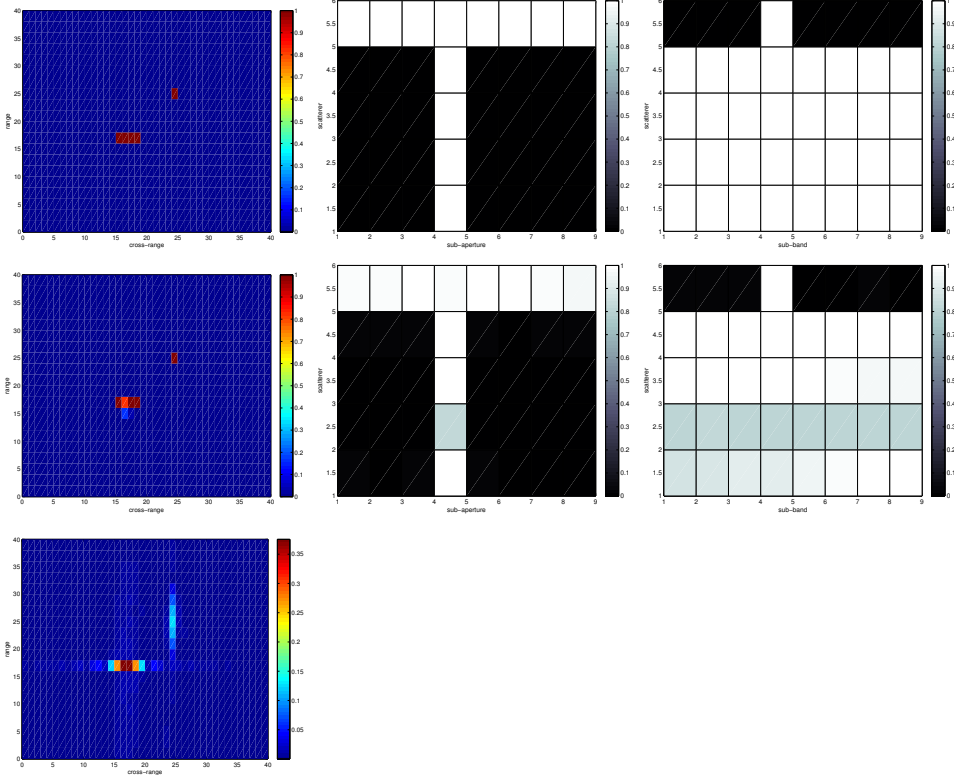
$$t = O(L/c) + O(1/B),$$

Fig. 5.7. *Results with $\mathcal{N}_\omega = 8$ frequency intervals, $\mathcal{N}_\alpha = 8$ apertures and data contaminated with 20% noise. On the top we show the true reflectivity as a function of location (left), direction (middle), and frequency (right). The reflectivity is supported in 5 pixels, four of them are adjacent and represent an extended scatterer, which is frequency independent. The other pixel supports a small scatterer with frequency dependent reflectivity. In the middle row we show the reconstructed reflectivity with the MMV algorithm. The plot in the bottom row is the migration image. The axes in the left images are cross-range and range in meters. The abscissa in the middle and right plots are the sub-aperture and sub-band index and the ordinate is the index of the pixel in the support of the scatterer.*

where L/c is the scale of the travel time and $1/B$ is the scale of the duration of the signal.

We conclude that the start stop approximation holds when

$$\omega_o t \gamma(s, \vec{y}) = O\Big(\frac{\omega_o L}{c}\frac{V}{c}\Big) + O\Big(\frac{\omega_o}{B}\frac{V}{c}\Big) \ll 1.$$

In the GOTCHA regime, considered in the numerical simulations in section 5, we have

$$\frac{\omega_o L}{c}\frac{V}{c} = 0.469, \qquad \frac{\omega_o}{B}\frac{V}{c} = 2.3 \cdot 10^{-5},$$

so $\omega_o t \gamma(s, \vec{y})$ is slightly less than one. We may include it in the data model, but it amounts to a constant additive phase that has no effect in imaging. To see this, let us take the Fourier transform with respect to t in (6.5)

$$\widehat{u}(s, \omega) \approx k^2 \int_\Omega d\vec{y} \rho(\vec{y}) \widehat{f}\Big[\omega\big(1 + 2\gamma(s, \vec{y})\big)\Big] \frac{\exp\big[2i\omega\big(1 + \gamma(s, \vec{y})\big)\tau(s, \vec{y})\big]}{(4\pi|\vec{r}(s) - \vec{y}|)^2}, \tag{6.6}$$

and expand the arguments over the slow time s and imaging point $\vec{y}$. We use the approximation

$$\vec{r}'(s) \approx V\Big[\vec{t}(s^\star) - \vec{n}(s^\star)\frac{V\Delta s}{R}\Big], \tag{6.7}$$

where Δs is the slow time offset from the center $s^\star$ of the aperture, and $\vec{t}(s^\star)$ is the unit tangent to the trajectory of the platform at the center point. The second term in (6.7) accounts for the curved platform trajectory, with

unit vector $\vec{\mathbf{n}}(s^\star)$ orthogonal to $\vec{\mathbf{t}}$, in the plane defined by $\vec{\mathbf{t}}$ and the center of curvature, and R the radius of curvature. We also have

$$|\vec{\mathbf{m}}(s,\vec{\mathbf{y}}) - \vec{\mathbf{m}}(s^\star,\vec{\mathbf{y}}_o)| = O\Big(\frac{V|\Delta s|}{L}\Big) + O\Big(\frac{|Y^\perp|}{L}\Big),$$

and

$$\omega_o\tau(s,\vec{\mathbf{y}}) = \omega_o\tau(s^\star,\vec{\mathbf{y}}_o) + O(k_o V \Delta s) + O(k_o \Delta y).$$

Substituting in (6.6) and using the parameters of the GOTCHA regime, we see that,

$$\omega\gamma(s,\vec{\mathbf{y}})\tau(s,\vec{\mathbf{y}}) \approx \omega_o\gamma(s^\star,\vec{\mathbf{y}}_o)\tau(s^\star,\vec{\mathbf{y}}_o),$$

so indeed, the Doppler effect amounts to a constant phase term.

6.2. Imaging algorithm with Doppler effects. The model of the down-ramped data with the Doppler correction follows from (6.6),

$$\begin{aligned}
d(s,\omega) &= \overline{\widehat{f}\big[\omega\big(1+2\gamma(s,\vec{\mathbf{y}}_o)\big)\big]}\,\widehat{u}(s,\omega)\exp\big[-2i\omega\big(1+\gamma(s,\vec{\mathbf{y}}_o)\big)\tau(s,\vec{\mathbf{y}}_o)\big] \\
&\approx k^2\,\overline{\widehat{f}\big[\omega\big(1+2\gamma(s,\vec{\mathbf{y}}_o)\big)\big]}\int_\Omega d\vec{\mathbf{y}}\,\widehat{f}\big[\omega\big(1+2\gamma(s,\vec{\mathbf{y}})\big)\big]\rho(\vec{\mathbf{y}})\times \\
&\quad \frac{\exp\big[2i\omega\big(1+\gamma(s,\vec{\mathbf{y}})\big)\tau(s,\vec{\mathbf{y}}) - 2i\omega\big(1+\gamma(s,\vec{\mathbf{y}}_o)\big)\tau(s,\vec{\mathbf{y}}_o)\big]}{\big(4\pi|\vec{\mathbf{r}}(s)-\vec{\mathbf{y}}|\big)^2}.
\end{aligned} \tag{6.8}$$

We are interested in direction and frequency dependent reflectivities, so to use formula (6.8), we consider next the $\alpha-$th sub-aperture and the $\beta-$th sub-band, where we can replace ρ by $\rho^{(\alpha,\beta)}(\vec{\mathbf{y}})$. The data is denoted by $d^{(\alpha,\beta)}(\Delta s, \Delta\omega)$, where $\Delta s = s - s_\alpha^\star$ and $\Delta\omega = \omega - \omega_\beta^\star$. The goal of the section is to include Doppler effects in the statements of Lemma 3.1 and Proposition 3.2, which are the basis of our imaging algorithm.

We begin with the observation that

$$\omega\gamma(s,\vec{\mathbf{y}})\tau(s,\vec{\mathbf{y}}) = \frac{\omega}{c}\frac{\vec{\mathbf{r}}'(s)}{c}\cdot(\vec{\mathbf{r}}(s)-\vec{\mathbf{y}}) = \omega\gamma(s,\vec{\mathbf{y}}_o)\tau(s,\vec{\mathbf{y}}_o) - \frac{\omega}{c}\frac{\vec{\mathbf{r}}'(s)}{c}\cdot\Delta\vec{\mathbf{y}}, \tag{6.9}$$

where $\Delta\vec{\mathbf{y}} = \vec{\mathbf{y}} - \vec{\mathbf{y}}_o$, and $\vec{\mathbf{r}}'(s)$ is given by (6.7), and assume henceforth that

$$\frac{V}{c}\frac{Y_\alpha^\perp}{L_\alpha} \ll \frac{b}{\omega_o} \ll 1. \tag{6.10}$$

This is consistent with our previous assumptions because $Y_\alpha^\perp \ll L_\alpha$ and $V \ll c$, and allows us to approximate the Doppler factor in the argument of the Fourier transform of the signal in (6.8) by its value at the reference point. Then, using equation (2.3) and noting also that

$$|\vec{\mathbf{r}}(s)-\vec{\mathbf{y}}| = L_\alpha\Big[1 + O\Big(\frac{a}{L_\alpha}\Big) + O\Big(\frac{Y_\alpha^\perp}{L_\alpha}\Big)\Big], \qquad k = k_o\Big[1 + O\Big(\frac{b}{\omega_o}\Big)\Big],$$

we can simplify the amplitude factor in (6.8) as

$$\frac{k^2\,\overline{\widehat{f}\big[\omega\big(1+2\gamma(s,\vec{\mathbf{y}}_o)\big)\big]}\,\widehat{f}\big[\omega\big(1+2\gamma(s,\vec{\mathbf{y}})\big)\big]}{(4\pi|\vec{\mathbf{r}}(s)-\vec{\mathbf{y}}|)^2} \approx \frac{k_o^2|\widehat{f}(\omega_o)|^2}{(4\pi L_\alpha)^2}, \tag{6.11}$$

and obtain

$$\begin{aligned}
d^{(\alpha,\beta)}(\Delta s, \Delta\omega) &\approx \frac{k_o^2|\widehat{f}(\omega_o)|^2}{(4\pi L_\alpha)^2}\sum_{q=1}^{Q}\rho_q^{(\alpha,\beta)}\exp\Big[-2i(k_\beta+\Delta k)\frac{\vec{\mathbf{r}}'(s_\alpha^\star+\Delta s)}{c}\cdot\Delta\vec{\mathbf{y}}_q + \\
&\quad 2i(\omega_\beta^\star+\Delta\omega)\big[\tau(s_\alpha^\star+\Delta s, \vec{\mathbf{y}}_o+\Delta\vec{\mathbf{y}}_q) - \tau(s_\alpha^\star+\Delta s, \vec{\mathbf{y}}_o)\big]\Big].
\end{aligned} \tag{6.12}$$

Here we have used that $k = k_\beta + \Delta k$, with center wavenumber $k_\beta = \omega_\beta^\star/c$ and offset $\Delta k = \Delta\omega/c$.

The difference between the travel times in the phase in (6.12) is approximated in the proof of Lemma 3.1 in appendix A. It remains to expand the first term in the phase, which is due to the Doppler factor. We use (6.7) and obtain

$$(k_\beta + \Delta k)\frac{\vec{\mathbf{r}}'(s_\alpha^\star + \Delta s)}{c} \cdot \Delta\vec{\mathbf{y}}_q = k_\beta \frac{V}{c}\left[\vec{\mathbf{t}}_\alpha \cdot \Delta\vec{\mathbf{y}}_q - \frac{V\Delta s}{R}\vec{\mathbf{n}}_\alpha \cdot \Delta\vec{\mathbf{y}}\right] + \Delta k \frac{V}{c}\vec{\mathbf{t}}_\alpha \cdot \Delta\vec{\mathbf{y}}_q +$$
$$O\left(\frac{V}{c}\frac{a}{R}\frac{\vec{\mathbf{n}}_\alpha \cdot \Delta\vec{\mathbf{y}}_q}{c/b}\right),$$

with negligible residual under the assumption

$$\frac{V}{c}\frac{a}{R}\frac{Y_\alpha}{c/b} \ll 1. \tag{6.13}$$

Recall that c/b is the range resolution, and although we want $Y_\alpha \gg c/b$, the inequality (6.13) is easily satisfied because $a \ll R \sim L_\alpha$ and $V \ll c$.

The generalization of the result in Lemma 3.1 is as follows. We have the linear system of equations

$$\mathbf{A}^{(\alpha,\beta)}\boldsymbol{\rho}^{(\alpha,\beta)} = \mathbf{d}^{(\alpha,\beta)}, \tag{6.14}$$

where the reflectivity vector $\boldsymbol{\rho}^{(\alpha,\beta)}$ with entries $\rho_q^{(\alpha,\beta)}$ is mapped to the data vector $\mathbf{d}^{(\alpha,\beta)}$ with entries $d^{(\alpha,\beta)}(\Delta s_j, \Delta\omega_l)$ by the reflectivity-to-data matrix $\mathbf{A}^{(\alpha,\beta)}$. The entries of $\mathbf{A}^{(\alpha,\beta)}$ are given by

$$A_{j,q}^{(\alpha,\beta)}(\Delta\omega_l) = \frac{k_o^2|\widehat{f}(\omega_o)|^2}{(4\pi L_\alpha)^2}\exp\left\{-2i(k_\beta + \Delta\omega_l/c)\left[\vec{\mathbf{m}}_\alpha \cdot \Delta\vec{\mathbf{y}}_q + \frac{V}{c}\vec{\mathbf{t}}_\alpha \cdot \Delta\vec{\mathbf{y}}_q\right]\right.$$
$$\left.-2i\frac{k_\beta V\Delta s}{L_\alpha}\left[\vec{\mathbf{t}}_\alpha \cdot \mathbb{P}_\alpha\Delta\vec{\mathbf{y}}_q - \frac{L_\alpha}{R}\frac{V}{c}\vec{\mathbf{n}}_\alpha \cdot \Delta\vec{\mathbf{y}}_q\right] + ik_\beta\frac{\Delta\vec{\mathbf{y}}_q \cdot \mathbb{P}_\alpha\Delta\vec{\mathbf{y}}_q}{L_\alpha}\right\}. \tag{6.15}$$

The difference between this reflectivity-to-data matrix and the one given by (3.12) in Lemma 3.1 comes from the V dependent terms in the square brackets in the phase, due to the Doppler effect.

We extend next the statement of Proposition 3.2. We proceed as in appendix A, and show that the matrix-matrix equation (3.1), $\mathbb{A}\mathbf{X} = \mathbf{D}$, still applies, with the same definition (3.17) of the data matrix $\mathbf{D}$,

$$D_j^{(\alpha,\beta)}(\Delta\omega_l) = \frac{(4\pi L_\alpha)^2}{k_o^2|\widehat{f}(\omega_o)|^2}d^{(\alpha,\beta)}(\Delta s_j, \Delta\omega_l),$$

and with the unknown matrix

$$X_q^{(\alpha,\beta)} = \rho_q^{(\alpha,\beta)}\exp\left\{-2ik_\beta\left[\frac{V}{c}\vec{\mathbf{t}}_\alpha \cdot \Delta\vec{\mathbf{y}}_q + \vec{\mathbf{m}}_\alpha \cdot \Delta\vec{\mathbf{y}}_q\right] + ik_\beta\frac{\Delta\vec{\mathbf{y}}_q \cdot \mathbb{P}_\alpha\Delta\vec{\mathbf{y}}_q}{L_\alpha}\right\}. \tag{6.16}$$

This is under the assumptions that

$$\max_{1\leq\alpha\leq\mathcal{N}_\alpha, 1\leq q\leq Q}\frac{V}{c}\frac{b}{c}\left|[\vec{\mathbf{t}}_\alpha - \vec{\mathbf{t}}_1] \cdot \Delta\vec{\mathbf{y}}_q\right| \ll 1, \tag{6.17}$$

$$\max_{1\leq\alpha\leq\mathcal{N}_\alpha, 1\leq q\leq Q}\frac{V}{c}\frac{a}{\lambda_o R}\left|(\vec{\mathbf{n}}_\alpha - \vec{\mathbf{n}}_1) \cdot \Delta\vec{\mathbf{y}}_q\right| \ll 1, \tag{6.18}$$

which are similar to (3.13)-(3.14), and easier to satisfy for smaller V. The expression of the entries of the reflectivity-to-data matrix is a simple modification of that in equation (3.19),

$$\mathbb{A}_{j,q}(\Delta\omega_l) = \exp\left[-2i\frac{\Delta\omega_l}{c}\left(\vec{\mathbf{m}}_1 \cdot \Delta\vec{\mathbf{y}}_q + \frac{V}{c}\vec{\mathbf{t}}_1 \cdot \Delta\vec{\mathbf{y}}_q\right)\right.$$
$$\left.-2ik_1\frac{V\Delta s_j}{L_1}\left(\vec{\mathbf{t}}_1 \cdot \mathbb{P}_1\Delta\vec{\mathbf{y}}_q - \frac{L_1}{R}\frac{V}{c}\vec{\mathbf{n}}_1 \cdot \Delta\vec{\mathbf{y}}_q\right)\right]. \tag{6.19}$$

Thus, the problem can be solved with the MMV approach, as described in section 4. The Doppler correction has two effects: It gives an extra rotation in the cross-range direction of the imaging window (the first phase term in (6.16), involving V), and two extra phase factors (involving V inside the parentheses) in the reflectivity-to-data matrix $\mathbb{A}$ in (6.19).

7. Summary. We have introduced and analyzed from first principles a synthetic aperture imaging approach for reconstructing direction and frequency dependent reflectivities of localized scatterers. It is based on two main ideas: The first one is to segment the data over subsets defined by carefully calibrated sub-apertures and frequency sub-bands, and formulate the reflectivity reconstruction for each subset as an ℓ_1 optimization problem. The direction and frequency dependence of the reconstructed reflectivity is frozen for each data subset but varies from one subset to another. The second idea is to fuse the sub-aperture and sub-band optimizations by seeking simultaneously from data subsets those reconstructions of the reflectivity that share the same spatial support in the image window. This is done with the multiple measurement vector (MMV) formalism, which leads to a matrix ℓ_1 optimization problem. The main result of this paper is showing that synthetic aperture imaging of direction and frequency dependent reflectivities can be formulated and solved efficiently as an MMV problem.

Data segmentation is a natural idea that has been used before for synthetic aperture imaging of frequency dependent reflectivities [21, 11]. Here we use it for estimating the direction dependence of the reflectivity, as well. We analyze how the size of the sub-apertures and frequency sub-bands in the data segmentation affects the resolution of the reconstructions as well as the computational complexity of the inversion. There is a trade-off in resolution in this approach: On one hand we want to have large sub-apertures and frequency sub-bands to get good spatial, range and cross-range, resolution of the reconstructed reflectivity. But on the other hand we also want to have small sub-apertures and frequency sub-bands to resolve well the direction and frequency dependence of the reflectivity. Small sub-apertures are also desirable so as to get images efficiently using Fourier transforms. The MMV formalism that we have introduced in this paper, and the associated algorithm for its implementation, deal well with these issues, as indicated by the numerical simulations.

Nearly all synthetic aperture imaging is done with reverse time migration algorithms, without regard to whether the reflectivities that are to be imaged are direction dependent or not. If the reflectivities are isotropic, then the spatial resolution of the reconstruction improves as the aperture increases. But this is not the case with direction dependent reflectivities as only part of the synthetic aperture will sense reflectivities from particular locations. This means that segmenting the data over sub-apertures is natural. The MMV-based imaging algorithm introduced in this paper handles automatically signals received by sub-apertures that are coming from directional reflectivities located in the image window.

Appendix A. Derivation of the reflectivity to data model. Here we show that the expression of $A_{j,q}(\omega_l)$ in (2.7) can be approximated by $A_{j,q}^{(\alpha,\beta)}(\Delta\omega_l)$ given in Lemma 3.1, for $\omega_l = \omega_\beta^\star + \Delta\omega_l$ and $s_j = s_\alpha^\star + \Delta s_j$. For simplicity of notation we drop the indexes j and l of the frequency and slowtime.

It is easy to see from (2.3) and the assumptions $\omega_o \gg b$ and $L_\alpha \gg a \gtrsim Y_\alpha$ that

$$\frac{k^2|\widehat{f}(\omega)|^2}{\left(4\pi|\vec{\mathbf{r}}(s) - \vec{\mathbf{y}}|\right)^2} \approx \frac{k_o^2|\widehat{f}(\omega_o)|^2}{(4\pi L_\alpha)^2}, \tag{A.1}$$

for $k = \omega/c$ and $k_o = \omega_o/c$. It remains to show the phase approximation

$$2\omega\left[\tau(s,\vec{\mathbf{y}}) - \tau(s,\vec{\mathbf{y}}_o)\right] \approx -2k\vec{\mathbf{m}}_\alpha \cdot \vec{\mathbf{y}} - 2k_\beta V\Delta s \frac{\vec{\mathbf{t}}_\alpha \cdot \mathbb{P}_\alpha\Delta\vec{\mathbf{y}}}{L_\alpha} + k_\beta \frac{\Delta\vec{\mathbf{y}} \cdot \mathbb{P}_\alpha\Delta\vec{\mathbf{y}}}{L_\alpha}, \tag{A.2}$$

where $\omega = \omega_\beta^\star + \Delta\omega$ lies in the frequency sub-band of width b, $s = s_\alpha^\star + \Delta s$ is in the sub-aperture of size a and $\vec{\mathbf{y}} = \vec{\mathbf{y}}_o + \Delta\vec{\mathbf{y}}$ is in $\mathcal{Y}$.

We begin by expanding the travel time in $\Delta\vec{\mathbf{y}}$,

$$\begin{aligned}
\Phi &= 2\omega\left[\tau(s,\vec{\mathbf{y}}) - \tau(s,\vec{\mathbf{y}}_o)\right] \\
&= -2k\vec{\mathbf{m}}(s,\vec{\mathbf{y}}_o) \cdot \Delta\vec{\mathbf{y}} + \frac{k}{|\vec{\mathbf{r}}(s) - \vec{\mathbf{y}}_o|}\Delta\vec{\mathbf{y}} \cdot \left[I - \vec{\mathbf{m}}(s,\vec{\mathbf{y}}_o)\vec{\mathbf{m}}^T(s,\vec{\mathbf{y}}_o)\right]\Delta\vec{\mathbf{y}} + \mathcal{E}_1,
\end{aligned}$$

19

with small residual

$$\mathcal{E}_1 = O\Big(\frac{{Y_\alpha^\perp}^2 Y_\alpha}{\lambda_o L_\alpha^2}\Big) \ll 1,$$

by assumption (3.10) and $Y_\alpha^\perp \lesssim a$, inferred from (3.7). Here we used the expression of the gradient

$$\nabla_{\vec{\mathbf{y}}}|\vec{\mathbf{r}}(s) - \vec{\mathbf{y}}| = -\frac{\vec{\mathbf{r}}(s) - \vec{\mathbf{y}}}{|\vec{\mathbf{r}}(s) - \vec{\mathbf{y}}|} = -\vec{\mathbf{m}}(s,\vec{\mathbf{y}}),$$

the Hessian

$$\nabla_{\vec{\mathbf{y}}} \otimes \nabla_{\vec{\mathbf{y}}}|\vec{\mathbf{r}}(s) - \vec{\mathbf{y}}| = \frac{1}{|\vec{\mathbf{r}}(s) - \vec{\mathbf{y}}|}\Big[I - \vec{\mathbf{m}}(s,\vec{\mathbf{y}})\vec{\mathbf{m}}^T(s,\vec{\mathbf{y}})\Big],$$

and

$$\sum_{i,j,q=1}^{3} \Delta y_i \Delta y_j \Delta y_q \partial^3_{y_i,y_j,y_q}|\vec{\mathbf{r}}(s) - \vec{\mathbf{y}}| = \frac{3\vec{\mathbf{m}}_\alpha \cdot \Delta\vec{\mathbf{y}}}{|\vec{\mathbf{r}}(s) - \vec{\mathbf{y}}|^2}\Big[|\Delta\vec{\mathbf{y}}|^2 - \big(\vec{\mathbf{m}}_\alpha \cdot \Delta\vec{\mathbf{y}}\big)^2\Big].$$

Next, we expand in $\Delta\omega = \omega - \omega_\beta^\star$ and obtain

$$\Phi = -2(k_\beta + \Delta k)\vec{\mathbf{m}}(s,\vec{\mathbf{y}}_o) \cdot \Delta\vec{\mathbf{y}} + \frac{k_\beta}{|\vec{\mathbf{r}}(s) - \vec{\mathbf{y}}_o|}\Delta\vec{\mathbf{y}} \cdot \big[I - \vec{\mathbf{m}}(s,\vec{\mathbf{y}}_o)\vec{\mathbf{m}}^T(s,\vec{\mathbf{y}}_o)\big]\Delta\vec{\mathbf{y}} + \mathcal{E}_2,$$

where $\Delta k = \Delta\omega/c$ and

$$\mathcal{E}_2 = \mathcal{E}_1 + O\Big(\frac{b}{\omega_o}\frac{{Y_\alpha^\perp}^2}{\lambda_o L_\alpha}\Big) \ll 1.$$

The last estimate is by assumption (3.9). Finally, we expand in $\Delta s = s - s_\alpha^\star$, and recalling the notation in section 3.1, we get

$$\Phi = -2(k_\beta + \Delta k)\vec{\mathbf{m}}_\alpha \cdot \Delta\vec{\mathbf{y}} - 2k_\beta\frac{V\Delta s}{L_\alpha}\vec{\mathbf{t}}_\alpha \cdot \mathbb{P}_\alpha\Delta\vec{\mathbf{y}} +$$
$$k_\beta\frac{\Delta\vec{\mathbf{y}} \cdot \mathbb{P}_\alpha\Delta\vec{\mathbf{y}}}{L_\alpha} + \mathcal{E}. \tag{A.3}$$

The residual is the sum of four terms

$$\mathcal{E} = \mathcal{E}_2 + \mathcal{E}_3 + \mathcal{E}_4 + \mathcal{E}_5,$$

with $\mathcal{E}_2$ given above. The term $\mathcal{E}_3$ comes from the quadratic part of the expansion of $k_\beta\vec{\mathbf{m}}(s,\vec{\mathbf{y}}_o) \cdot \Delta\vec{\mathbf{y}}$,

$$\mathcal{E}_3 \sim k_\beta(V\Delta s)^2\Big[\frac{\vec{\mathbf{n}}_\alpha \cdot \mathbb{P}_\alpha\Delta\vec{\mathbf{y}}}{RL_\alpha} + \frac{\vec{\mathbf{t}}_\alpha \cdot \big[\vec{\mathbf{m}}_\alpha' \vec{\mathbf{m}}_\alpha^T + \vec{\mathbf{m}}_\alpha(\vec{\mathbf{m}}_\alpha')^T\big]\Delta\vec{\mathbf{y}}}{VL_\alpha} + \frac{\big(\vec{\mathbf{t}}_\alpha \cdot \mathbb{P}_\alpha\Delta\vec{\mathbf{y}}\big)\big(\vec{\mathbf{t}}_\alpha \cdot \vec{\mathbf{m}}_\alpha\big)}{L_\alpha^3}\Big].$$

Here $\sim$ denotes order of magnitude, and the primes denote derivative with respect to s. The unit vector $\vec{\mathbf{n}}_\alpha$ is normal to $\vec{\mathbf{t}}_\alpha$, in the plane defined by $\vec{\mathbf{t}}_\alpha$ and the center of curvature of the trajectory of the platform. It enters the definition

$$\vec{\mathbf{t}}_\alpha' = -\frac{V\vec{\mathbf{n}}_\alpha}{R}, \tag{A.4}$$

where $R \sim L_\alpha$ is the radius of curvature. Moreover

$$\vec{\mathbf{m}}_\alpha' = \frac{V}{L_\alpha}\mathbb{P}_\alpha\vec{\mathbf{t}}_\alpha. \tag{A.5}$$

We conclude that

$$\mathcal{E}_3 = O\Big(\frac{a^2 Y_\alpha^\perp}{\lambda_o L_\alpha^2}\Big) + O\Big(\frac{a^2 Y_\alpha}{\lambda_o L_\alpha^2}\Big) \ll 1,$$

where the inequality is by assumption (3.10).

The term $\mathcal{E}_4$ in the residual is

$$\mathcal{E}_4 \sim \frac{\Delta\omega}{c}\frac{V\Delta s}{L_\alpha}\vec{\mathbf{t}}_\alpha \cdot \mathbb{P}_\alpha\Delta\vec{\mathbf{y}} = O\Big(\frac{b}{\omega_o}\frac{aY_\alpha^\perp}{\lambda_o L_\alpha}\Big) \ll 1,$$

by assumption (3.9), and the last term $\mathcal{E}_5$ comes from the expansion of the quadratic term in $\Delta\vec{\mathbf{y}}$ in the expression of Φ. We estimate it as

$$\mathcal{E}_5 = O\Big(\frac{aY_\alpha Y_\alpha^\perp}{\lambda_o L_\alpha^2}\Big) \ll 1,$$

where we used assumption (3.10). The statement of Lemma 3.1 follows from (A.1) and (A.3). $\square$

Proposition 3.2 follows easily from the expression (3.1) of $A_{j,q}^{(\alpha,\beta)}$ and assumptions (3.13) and (3.14). Writing the linear system (3.11) componentwise we get

$$\sum_{q=1}^{Q} X_q^{(\alpha,\beta)} \exp\Big[-2i\frac{\Delta\omega_l}{c}\vec{\mathbf{m}}_\alpha \cdot \vec{\mathbf{y}}_q - 2ik_\beta V\Delta s_j \frac{\vec{\mathbf{t}}_\alpha \cdot \mathbb{P}_\alpha \Delta\vec{\mathbf{y}}_q}{L_\alpha}\Big] = D_j^{(\alpha,\beta)}(\Delta\omega_l),$$

with $X_q^{(\alpha,\beta)}$ given in (3.15) and $D_j^{(\alpha,\beta)}$ defined in (3.17). The result (3.19) follows from this equation and assumptions (3.13) and (3.14). $\square$

Appendix B. Inner products for rows and columns of the reflectivity-to-data matrix.

Here we analyze the relation between the discretization of the imaging window $\mathcal{Y}$ and the linear independence of the columns of the reflectivity to data matrix. This is done by computing inner products of of normalized rows and columns of the reflectivity-to-data matrix. If the column inner products multiplied by the number of elements in the support of the reflectivities are below a threshold then the MMV algorithm will give an exact reconstruction, in the noiseless case [5].

We consider the restriction to a data subset, defined by a sub-aperture and frequency sub-band satisfying the assumptions in section 3. Thus, we work with matrices $\mathbf{A}^{(\alpha,\beta)}$, but to simplify notation we drop the indexes (α, β).

Let us denote by $\mathbf{a}_q$ the $q-$th column of matrix $\mathbf{A}$ and calculate the inner product

$$\langle \mathbf{a}_q, \mathbf{a}_{q'} \rangle = \Big(\mathbf{A}^\star \mathbf{A}\Big)_{q,q'} = \sum_{j=1}^{n_s}\sum_{l=1}^{n_\omega} \overline{A_{j,q}(\Delta\omega_l)} A_{j,q'}(\Delta\omega_l).$$

Using Lemma 3.1 we get

$$\Big\langle \frac{\mathbf{a}_q}{\|\mathbf{a}_q\|}, \frac{\mathbf{a}_{q'}}{\|\mathbf{a}_{q'}\|} \Big\rangle = \exp\Big[-2ik_\beta\vec{\mathbf{m}}_\alpha \cdot (\vec{\mathbf{y}}_{q'} - \vec{\mathbf{y}}_q) + \frac{ik_\beta\Big(\Delta\vec{\mathbf{y}}_{q'}\mathbb{P}_\alpha\Delta\vec{\mathbf{y}}_{q'} - \Delta\vec{\mathbf{y}}_q\mathbb{P}_\alpha\Delta\vec{\mathbf{y}}_q\Big)}{L_\alpha}\Big] \times$$
$$\frac{1}{n_s n_\omega}\sum_{j=1}^{n_s}\sum_{l=1}^{n_\omega}\exp\Big[-\frac{2i\Delta\omega_l}{c}\vec{\mathbf{m}}_\alpha \cdot (\vec{\mathbf{y}}_{q'} - \vec{\mathbf{y}}_q) - \frac{2ik_\beta V\Delta s_j}{L_\alpha}\vec{\mathbf{t}}_\alpha \cdot \mathbb{P}_\alpha(\vec{\mathbf{y}}_{q'} - \vec{\mathbf{y}}_q)\Big],$$

where we normalized the columns by their Euclidian norm. The sums can be approximated by integrals over the frequency band and aperture, as long as they are sampled at intervals h_ω and h_s satisfying

$$\frac{h_\omega}{b}\frac{|\vec{\mathbf{m}}_\alpha \cdot (\vec{\mathbf{y}}_q - \vec{\mathbf{y}}_{q'})|}{c/b} \ll 1, \qquad \frac{Vh_s}{a}\frac{|\vec{\mathbf{t}}_\alpha \cdot \mathbb{P}_\alpha(\vec{\mathbf{y}}_{q'} - \vec{\mathbf{y}}_q)|}{\lambda_o L/a} \ll 1.$$

We obtain after taking absolute values that

$$\Big|\Big\langle \frac{\mathbf{a}_q}{\|\mathbf{a}_q\|}, \frac{\mathbf{a}_{q'}}{\|\mathbf{a}_{q'}\|} \Big\rangle\Big| \approx \Big|\mathrm{sinc}\Big(\frac{b}{c}\vec{\mathbf{m}}_\alpha \cdot (\vec{\mathbf{y}}_{q'} - \vec{\mathbf{y}}_q)\Big)\mathrm{sinc}\Big(\frac{k_o a}{L_\alpha}\vec{\mathbf{t}}_\alpha \cdot \mathbb{P}_\alpha(\vec{\mathbf{y}}_{q'} - \vec{\mathbf{y}}_q)\Big)\Big|. \tag{B.1}$$

This is small for $q \neq q'$ when we sample the imaging window $\mathcal{Y}$ in steps that are larger than the resolution limits c/b in range and $\lambda_o L/a$ in cross-range.

21

A similar calculation can be done for the rows of $\mathbf{A}$, denoted by $\mathbf{a}_{(j,l)}$. We have

$$\left\langle \mathbf{a}_{(j',l')}, \mathbf{a}_{(j,l)} \right\rangle = \left(\mathbf{A}\mathbf{A}^* \right)_{(j,l),(j',l')} = \sum_{q=1}^{Q} \overline{A_{j',q}(\Delta\omega_{l'})} A_{j,q}(\Delta\omega_l),$$

and using Lemma 3.1 we get

$$\left| \left\langle \frac{\mathbf{a}_{(j',l')}}{\|\mathbf{a}_{(j',l')}\|}, \frac{\mathbf{a}_{(j',l')}}{\|\mathbf{a}_{(j',l')}\|} \right\rangle \right| = \frac{1}{Q} \sum_{q=1}^{Q} \exp\left[\frac{2i(\omega_{l'} - \omega_l)\vec{\mathbf{m}}_\alpha \cdot \Delta\vec{\mathbf{y}}_q}{c} + \frac{2ik_\beta V(s_{j'} - s_j)\vec{\mathbf{t}}_\alpha \cdot \mathbb{P}_\alpha \Delta\vec{\mathbf{y}}_q}{L_\alpha} \right].$$

Furthermore, for discretizations of the imaging window in steps h in range and $h^\perp$ in cross-range, satisfying

$$\frac{|\omega_{l'} - \omega_l|}{b} \frac{h}{c/b} \ll 1, \qquad \frac{V|s_j - s_{j'}|}{a} \frac{h^\perp}{\lambda_o L_\alpha/a} \ll 1,$$

we can approximate the sum over q by an integral over the imaging window and obtain

$$\left| \left\langle \frac{\mathbf{a}_{(j',l')}}{\|\mathbf{a}_{(j',l')}\|}, \frac{\mathbf{a}_{(j',l')}}{\|\mathbf{a}_{(j',l')}\|} \right\rangle \right| \approx \left| \mathrm{sinc}\left(\frac{(\omega_{l'} - \omega_l)Y_\alpha}{c} \right) \mathrm{sinc}\left(\frac{k_o V(s_{j'} - s_j)Y_\alpha^\perp}{L_\alpha} \right) \right|.$$

This result shows that the inner product of the rows is small when the frequency is sampled in steps larger than Y_α/c and the slow time is sampled in steps larger than $(1/V)/(\lambda_o Y_\alpha^\perp/L_\alpha)$.

REFERENCES

[1] R. Baraniuk and P. Steeghs, *Compressive radar imaging*, in Radar Conference, 2007 IEEE, IEEE, 2007, pp. 128–133. 2, 4
[2] L. Borcea and I. Kocyigit, *Resolution analysis of imaging with l1 optimization*, arXiv preprint arXiv:1507.00586, (2015). 2, 4, 10
[3] C. Casteel Jr, L. Gorham, M. Minardi, S. Scarborough, K. Naidu, and U. Majumder, *A challenge problem for 2d/3d imaging of targets from a volumetric data set in an urban environment*, in Proceedings of SPIE, vol. 6568, 2007, p. 65680D. 9
[4] A. Chai, M. Moscoso, and G. Papanicolaou, *Robust imaging of localized scatterers using the singular value decomposition and l1 minimization*, Inverse Problems, 29 (2013), p. 025016. 2, 4
[5] ———, *Imaging strong localized scatterers with sparsity promoting optimization*, SIAM Journal on Imaging Sciences, 7 (2014), pp. 1358–1387. 2, 4, 9, 21
[6] J. Chen and X. Huo, *Theoretical results on sparse representations of multiple-measurement vectors*, Signal Processing, IEEE Transactions on, 54 (2006), pp. 4634–4643. 8
[7] M. Cheney, *A mathematical tutorial on synthetic aperture radar*, SIAM review, 43 (2001), pp. 301–312. 1
[8] M. Cheney, *Imaging frequency-dependent reflectivity from synthetic-aperture radar*, Inverse Problems, 29 (2013), p. 054002. 1
[9] S. F. Cotter, B. D. Rao, K. Engan, and K. Kreutz-Delgado, *Sparse solutions to linear inverse problems with multiple measurement vectors*, Signal Processing, IEEE Transactions on, 53 (2005), pp. 2477–2488. 2, 8
[10] J. C. Curlander and R. N. McDonough, *Synthetic Aperture Radar: Systems and Signal Processing*, Wiley-Interscience, 1991. 1
[11] C. Elachi, Y. Kuga, K. McDonald, K. Sarabandi, F. Ulaby, M. Whitt, H. Zebker, and J. van Zyl, *Radar polarimetry for geoscience applications*, Norwood, MA (USA); Artech House Inc., 1990. 1, 19
[12] Y. Eldar and H. Rauhut, *Average case analysis of multichannel sparse recovery using convex relaxation*, Information Theory, IEEE Transactions on, 56 (2010), pp. 505–519. 8, 9
[13] A. C. Fannjiang and W. Liao, *Coherence pattern-guided compressive sensing with unresolved grids*, SIAM Journal on Imaging Sciences, 5 (2012), pp. 179–202. 2, 4
[14] A. C. Fannjiang, T. Strohmer, and P. Yan, *Compressed remote sensing of sparse objects*, SIAM Journal on Imaging Sciences, 3 (2010), pp. 595–618. 2, 4
[15] C. V. J. Jr., D. E. Wahl, P. H. Eichel, D. C. Ghiglia, and P. A. Thompson, *Spotlight-mode synthetic aperture radar: A signal processing approach*, Springer, New York, NY, 1996. 1
[16] D. Malioutov, M. Cetin, and A. Willsky, *A sparse signal reconstruction perspective for source localization with sensor arrays*, Signal Processing, IEEE Transactions on, 53 (2005), pp. 3010–3022. 2, 9
[17] M. Moscoso, A. Novikov, G. Papanicolaou, and L. Ryzhik, *A differential equations approach to l 1 -minimization with applications to array imaging*, Inverse Problems, 28 (2012), p. 105001. 9
[18] L. C. Potter, E. Ertin, J. T. Parker, and M. Cetin, *Sparsity and compressed sensing in radar imaging*, Proceedings of the IEEE, 98 (2010), pp. 1006–1020. 2, 4
[19] B. Rao and K. Kreutz-Delgado, *Sparse solutions to linear inverse problems with multiple measurement vectors*, in Proceedings of the 8th IEEE Digital Signal Processing Workshop, 1998. 8

[20] M. I. Skolnik, *Radar handbook*, McGraw-Hill, 3 ed., 2008. 1, 3

[21] P. Sotirelis, J. T. Parker, M. Fu, X. Hu, and R. Albanese, *A study of material identification using sar*, in Radar Conference (RADAR), 2012 IEEE, IEEE, 2012, pp. 0112–0115. 1, 19

[22] J. A. Tropp, *Algorithms for simultaneous sparse approximation. part ii: Convex relaxation*, Signal Processing, 86 (2006), pp. 589–602. 2

[23] J. A. Tropp, A. C. Gilbert, and M. J. Strauss, *Algorithms for simultaneous sparse approximation. part i: Greedy pursuit*, Signal Processing, 86 (2006), pp. 572–588. 2